공학박사 학위논문

Automatic Heart Segmentation using Gradient-assisted Localized Active Contour in Cardiac CT Images

심장 컴퓨터 단층촬영 영상으로부터 경사도 보조 지역 능동 윤곽 모델을 이용한 심장 영역 자동 분할 기법

2015년 2월

서울대학교 대학원

전기컴퓨터공학부

강 호 철

Automatic Heart Segmentation using Gradient-assisted Localized Active Contour in Cardiac CT Images

지도교수 신 영 길

이 논문을 공학박사 학위논문으로 제출함
2015년 1월

서울대학교 대학원
전기컴퓨터공학부
강 호 철

강호철의 박사 학위논문을 인준함
2015년 1월

위 원 장 김 명 수 (인)

부위원장 신 영 길 (인)

위 원 서 진 욱 (인)

위 원 김 보 형 (인)

위 원 이 정 진 (인)

Abstract

Automatic Heart Segmentation using Gradient-assisted Localized Active Contour in Cardiac CT Images

Ho Chul Kang

Department of Computer Science and Engineering

The Graduate School

Seoul National University

The heart is one of the most important human organs, and composed of complex structures. Computed tomography angiography (CTA), magnetic resonance imaging (MRI), and single photon emission computed tomography are widely used, non-invasive cardiac imaging modalities. Compared with other modalities, CTA can provide more detailed anatomic information of the heart chambers, vessels, and coronary arteries due to its higher spatial resolution. To obtain important morphological information of the heart, whole heart segmentation is necessary and it can be used for clinical diagnosis. In this paper, we propose a novel framework to segment the four chambers of the heart automatically. First, the whole heart is coarsely extracted. This is separated into the left and right parts using a geometric analysis based on anatomical information and a subsequent power watershed. Then, the proposed gradient-assisted localized active contour model (GLACM) refines the left and right sides of the heart segmentation accurately. Finally, the left and right sides of the heart are separated into atrium and ventricle by minimizing the proposed split energy function that determines the boundary between the atrium and ventricle based on the shape and intensity of the heart. The main challenge of heart segmentation is to extract four chambers from

cardiac CTA which has weak edges or separators. To enhance the accuracy of the heart segmentation, we use region-based information and edge-based information for the robustness of the accuracy in heterogeneous region. Model-based method, which requires a number of training data and proper template model, has been widely used for heat segmentation. It is difficult to model those data, since training data should describe precise heart regions and the number of data should be high in order to produce more accurate segmentation results. Besides, the training data are required to be represented with remarkable features, which are generated by manual setting, and these features must have correspondence for each other. However in our proposed methods, the training data and template model is not necessary. Instead, we use edge, intensity and shape information from cardiac CTA for each chamber segmentation. The intensity information of CTA can be substituted for the shape information of the template model. In addition, we devised adaptive radius function and Gaussian-pyramid edge map for GLACM in order to utilize the edge information effectively and improve the accuracy of segmentation comparison with original localizing region-based active contour model (LACM). Since the radius of LACM affects the overall segmentation performance, we proposed an energy function for changing radius adaptively whether homogeneous or heterogeneous region. Also we proposed split energy function in order to segment four chambers of the heart in cardiac CT images and detects the valve of atrium and ventricle. In experimental results using twenty clinical datasets, the proposed method identified the four chambers accurately and efficiently. We also demonstrated that this approach can assist the cardiologist for the clinical investigations and functional analysis.

Keywords: Heart segmentation, four-chamber segmentation, localized active contour model, edge map, split energy function

Student Number: 2009-30909

Contents

List of Tables

List of Figures

Chapter 1. Introduction

1.1 Background and Motivation

Computed tomography (CT) is an imaging procedure that uses x-ray technology to produce tomographic images of specific object. To produce CT volume of data, the patient is placed into a tube. This tube emits x-rays toward the center of the cylinder. The x-rays pass through the body and the intensity is measured on the other side. Then a reconstruction work is done to actually obtain a 3D image. CT distinguishes bones better than organic tissues. The muscle and the cavities of the specific organ are not well differentiated, both appearing on close gray tones on the CT scan.

The heart is a muscular organ about the size of a closed fist that functions as the body's circulatory pump. It takes in deoxygenated blood through the veins and delivers it to the lungs for oxygenation before pumping it into the various arteries (which provide oxygen and nutrients to body tissues by transporting the blood throughout the body). The heart is located in the thoracic cavity medial to the lungs and posterior to the sternum (see Figure 1.1).

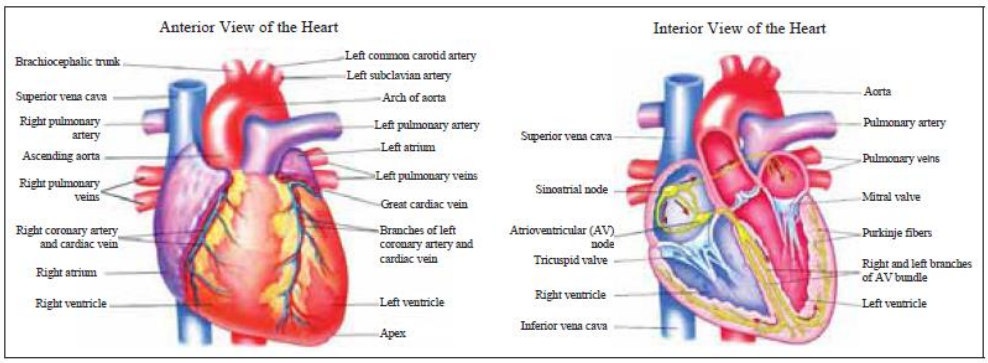

Figure 1.1 Heart anatomy from the anterior view (left) and interior view (right) [51]

Computed tomography angiography (CTA), magnetic resonance imaging (MRI), and single photon emission computed tomography are widely used, non-invasive cardiac imaging modalities. Compared with other modalities, CTA can provide more detailed anatomic information of the heart chambers, vessels, and coronary arteries due to its higher spatial resolution [1].

Disorders of the heart or blood vessels often cause cardiovascular diseases including coronary heart disease, cerebrovascular disease, elevated blood pressure, peripheral artery disease, rheumatic heart disease, congenital heart disease, and heart failure [2]. For the early diagnosis of these cardiovascular diseases, CTA has been increasingly used. Cardiac flow analysis including the quantification and visualization of the cardiac flow, are important to understand blood dynamics within the heart and detect cardiac abnormalities [3, 4]. It is difficult due to the complexity of blood dynamics and myocardial motion so that computerized image

processing is necessary and 3D visualization of cardiac flow is also important [5].

There have been a number of studies for cardiovascular segmentation and analysis. Lesage et al. [6] reviewed various vascular segmentation methods. Most of these methods require user interaction such as seed points for the start and end points of a vessel. Boskamp et al. [7] proposed a vessel segmentation method based on region growing algorithm. This method is sensitive to noise and weak in heterogeneous region. Mille and Cohen [8] present 2D and 3D extraction and reconstruction of branching structures for a deformable tree model. They utilized explicit active contour model, evolving a centerline curve with varying radius of the curve. Luboz et al. [9] proposed a method for the segmentation and reconstruction of human vascular structures by using level set evolution. Although it has been an amount of past and on-going research for cardiovascular segmentation and analysis, cardiac segmentation of the four chambers still remains a challenging task.

Cardiac segmentation of the four chambers is a prerequisite for the clinical investigations and quantitative, functional analysis of the ventricle and atrium [10]. The majority of previous studies have focused on the segmentation of the left ventricle (LV); the diastolic and systolic LV volumetrics are important factors in predicting heart diseases [11]. The requirement for the automatic segmentation of the four cardiac chambers has recently increased because it provides useful

information for cardiac diseases in other chambers, such as left atrial fibrillation and right ventricular overload [12]. However, it is very difficult to segment the four chambers because it is hard to detect the valves that separate the ventricle/atrium or artery/chamber owing to the similar intensity of nearby objects. In addition, the region of each chamber is inhomogeneous due to the irregular characteristics of angiography, making the segmentation more difficult.

The active contour model has been widely used to segment organs in medical imaging. Wong et al. [13, 14] proposed cardiac chamber segmentation method using active contour model for cardiac flow analysis. Since it is difficult to segment cardiac chambers automatically which have weak boundary, they implemented a semi-automatic segmentation algorithm when the automatic segmentation was failed. Tan et al. [15] presented an eye, cornea and ocular surface detection algorithm using active contour model [16] with gradient vector flow (GVF) and genetic algorithm. GVF is an external force field of active contour model and able to converge to boundary concavities. Therefore, it is not necessary for the initial contour to be close to the boundary, and this algorithm does not need any human intervention.

Several approaches for the automatic segmentation of the four chambers have been researched. Most of these approaches exploit the model-based methods, such as the active shape model (ASM) [17], active appearance model (AAM) [18], and

deformable model [19, 20]. ASM uses a statistical shape model and a matching algorithm between the model and real clinical data. AAM exploits the image appearance and the object shape in a set of training data as a statistical shape-appearance model. Assen et al. [21] proposed an automatic segmentation using three-dimensional (3D) ASM in cardiac MRI. Relative gray-level differences instead of absolute gray values were used for the classification of the 3D regions of interest. However, this method required the further generalization of the fuzzy inference system [22] and segmented only the LV and myocardium. Mitchell et al. [23] developed a model-based segmentation method using 3D AAM. This did not require any interactive user input of cardiac MRI and echocardiographic temporal image sequences. This method did require a number of training data sets from manually traced segmentation results. Ecabert et al. [24] proposed a fully automatic segmentation of the four chambers using a statistical, cardiac geometry model and training meshes from cardiac CTA images. This method required well-defined training data sets and excessive time and effort to generate the template mesh.

Funka-Lea et al. [25] developed the method to automatically isolate the outer boundary of the entire heart using balloon expansion and graph-cut technique. This approach extracted only the whole heart, not four chambers. Grady et al. [26] evaluated three techniques, graph cuts, isoperimetric minimization and random walks for the segmentation of four chambers. However, these methods extracted

four chambers with the input of seed points for each chamber and a lot of seed points were required for the accurate segmentation results.

Zheng et al. [27] developed an automatic four-chamber heart segmentation system using marginal space learning (MSL) and steerable features. MSL is introduced to solve the 9-D similarity-transformation search problem for localizing the heart chambers and to estimate the shape through learning-based boundary delineation. This model is an efficient and robust approach for automatic heart-chamber segmentation. However, the triangulated surface mesh and training data must be set. Zhang et al. [28] developed a novel sparse-shape composition model that uses a shape repository consisting of a number of annotated shape instances. It is inspired by the sparsity theory in compressive sensing. This method requires a selection and combination of a sparse set of shapes from the shape repository.

Olivier et al. [29] suggested a heart segmentation method using an iterative Chan-Vese algorithm [30]. They used an L1 fidelity term for the computational efficiency instead of L2 fidelity. However, this approach extracted only the whole heart and did not segment each chamber. H. A. Kirisl et al. [12] proposed a multi-atlas-based cardiac segmentation using a non-rigid registration technique. This fully automatic method for segmenting cardiac chambers uses eight atlas models. Each registered image is combined and used for the generation of the final segmentation result. However, this method requires a long processing time due to

the sequential and computationally expensive registration stages.

1.2 Dissertation Goals

This paper proposes a method that automatically extracts the four chambers from a cardiac CTA (see figure 1.2). First, we roughly segment the whole heart based on intensity. The heart is split into left and right parts by a geometric analysis based on anatomical information and a subsequent power watershed. Then, the left and right sides of the heart are accurately segmented by our gradient-assisted localized active contour model (GLACM) that considers both region and edge-based information. Active contour model with edge-based information has some limitations which are very sensitive to image noise and dependent on the initial contour. Region-based active contour models compensate these problems using the global statistics between foreground and background regions [30]. However, region-based methods are very weak in heterogeneous objects due to the consideration of global information only. To solve this problem, we add the edge-based term to our energy model for considering local information. Within GLACM, we present an energy function in terms of the circular region with an adaptively changed radius that determines the range of segmentation. In the localizing region-based active contour model (LACM) [31], only the points within the circle having

a constant radius, whose center is located on the contour, are considered. In GLACM, we consider the points within the circle having an adaptively changed radius. Finally, the regions of the left and right sides of the heart are separated into the ventricle and atrium by the proposed split energy function based on the shape and intensity of the heart. This function allows the heart to be robustly divided into each chamber even in the case of having a weak edge.

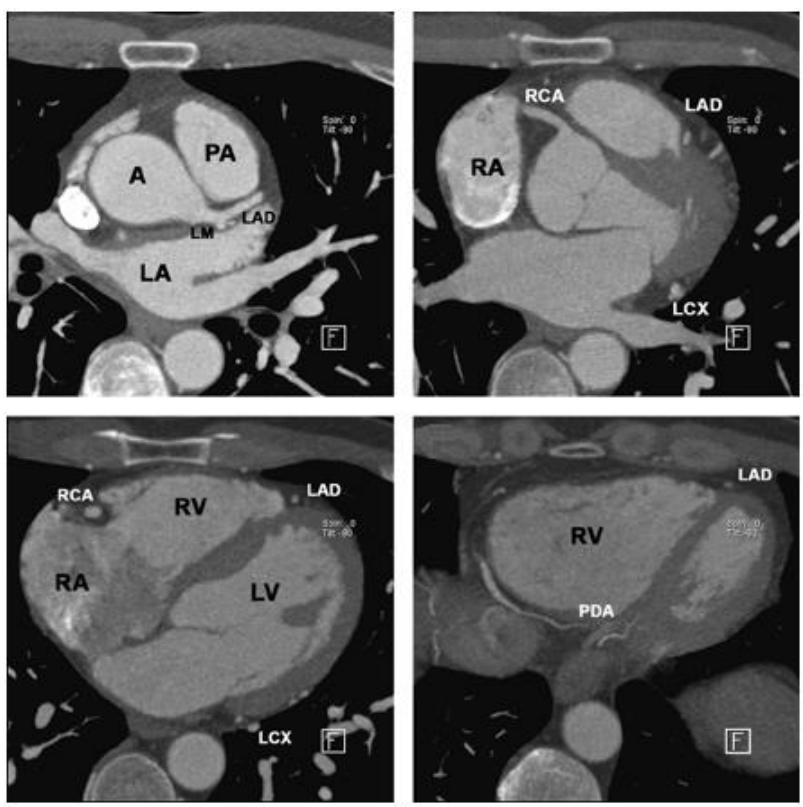

Figure 1.2 Four chambers in cardiac CT images. LV (left ventricle), LA (left atrium), RV (right ventricle), and RA (right atrium)

1.3 Main Contribution

The purpose of this study is to develop automatic four-chamber segmentation of the heart that applies Gradient-assisted LACM (GLACM) and split energy function. To improve the accuracy of the heart segmentation, we use not only region-based information but also edge-based information for the robustness of the accuracy in heterogeneous region.

Since existing methods used model-based method, a number of training data and proper template model of heart should be required in order to produce more accurate segmentation results. Meanwhile, the training data and template model is not necessary to our proposed method. Instead, we use edge, intensity and shape information from cardiac CTA for each chamber segmentation.

In addition, we propose adaptive radius function and Gaussian-pyramid edge map for GLACM in order to improve the accuracy of segmentation comparison with classic LACM. The proposed method was applied to segment four chambers of the heart in cardiac CT images and detects the valve of atrium and ventricle while using split energy function.

1.4 Organization of the Dissertation

The organization of the dissertation is as follows. The Chapter 2 gives the related works in medical image segmentation and heart segmentation. In Chapter 3, we describe a proposed method, GLACM. We introduce classic LACM, and describe our method including Gaussian-pyramid edge map, adaptive radius function and split energy function. In Chapter 4, the overall workflow of the four-chamber segmentation is described. This procedure consists of four processing steps. Chapter 5 presents the experimental results of this study. Finally, we summarize the results and discuss future work in Chapter 6.

Chapter 2. Related Works

In this Chapter, we briefly introduce the related works about medical image segmentation and heart segmentation. In Section 2.1, we review the medical image segmentation methods from most simple techniques to more recent techniques by means of optimizing energy functional. In Section 2.2 we review the heart segmentation including four-chamber segmentation.

2.1 Medical image Segmentation

2.1.1 Classic Method

A number of approaches for the automatic and semi-automatic segmentation have been researched for a long time. The early and simple method of segmentation generally used the assumption that relevant objects in the image can be classified based on intensity values and each object is composed of homogeneous region. The one of the most simple segmentation method is to use a single threshold value, such that pixels less and greater than the threshold are

object pixels and background pixels respectively because object normally has higher intensity value and background has lower intensity value. This method works well for high contrast objects with a sharp edge. There are another classic methods, edge detection, Hough transformation and region growing.

Threshold: Threshold is one of the most ancient and simple methods in image segmentation. From a grayscale image, thresholding is used to generate binary image which includes the data of object. We can use threshold which is intensity value to segment a region of interest (ROI) in the image. A good threshold demand that the intensity distribution of the ROI should not be overlapping with other regions in the image histogram. So to make the accuracy of segmentation more robust, the threshold should be automatically selected by automatic thresholding method, e.g. Otsu thresholding [33]. Otsu's method uses that a measure of region homogeneity is variance, i.e., regions of high homogeneity have low variance. It selects the threshold by minimizing the within-class variance of the two class separated by the threshold. It assumes a bimodal distribution of grayscale values. Knowledge about the objects, the application and the environment should be used to choose the threshold automatically, intensity characteristics of the objects, sizes of the objects, number of different types of objects, etc. In the heart segmentation, especially myocardium, might be extracted improperly only with thresholding,

since the intensity of the myocardium has similar value as liver or left ventricle which has irregular characteristics of angiography. In addition, the separation of the blood pool into different anatomical regions, such as the right atrium and ventricle segmentation is very difficult. The intensity range of the atrial blood cavities is similar as the range of the ventricular blood cavities. And this method often fails as soon as the edges are smooth, varying intensity and influenced by noise.

Edge detection: Edge is significant local changes of intensity in the image. It generally occur on the boundary between two different object or regions in the image. The goal of edge detection is to produce a line drawing of a scene from the image and extracts important features from the edges. Edge detection takes the intensity values of neighbor points into consideration when deciding the boundaries between regions. There have been proposed a number of studies for edge detection [52]. High magnitude of intensity gradient is usually considered as having a high probability of being edge points and edges can be modeled according to their intensity profiles. The simplest method of edge detection is to use Sobel operation. The Sobel filter is used in image processing and computer vision in order to detect edge and create an image with emphasizes edges. The operator uses two 3x3 kernels which are convolved with the original image to calculate approximations of the derivatives, i.e. horizontal and vertical changes. Canny [53] proposed that

points with local maximal gradient, zero second directional derivatives, should be edge candidates. It makes the edge detection be more easy and robust to noise using a technique, known as hysteresis, to protect true edge with low magnitude of intensity gradient.

Hough transformation: Circle is one of the common geometric structures in image processing and computer vision application, especially feature detection and segmentation. Hough transformation (HT) [54] is used to detect lines and circles. It is a particular example of the use the HT to search a parameter space. In other words, the HT method of shape analysis uses a constraint equation relating points in a feature space to possible parameter values of the searched for shape. It is used to determine the parameters of a circle with the parametric equation w.r.t. the radius of circle and center when a number of points that fall on the perimeter are known. If an image contains many points which include circle, then the circle detection algorithm is progressed by finding parameter triplets (the center of x, the center of y, the radius of circle) to describe each circle. Its drawback is its inability to detect concentric circles.

Region growing: Region growing [55] incorporates the knowledge that pixels in the same region are connected and have a similar intensity value. It is the

opposite of the split and merge approach, and this approach is assumed in the procedure of growing the region. First, an initial set of small areas are interactively merged according to similarity constraints, then start by choosing an arbitrary seed pixel and compare it with neighboring pixels. Region is grown from the seed pixel by adding in neighboring pixels that are similar, increasing the size of the region. Finally, when the growth of one region stops we simply choose another seed pixel which does not yet belong to any region and start again. This whole process is continued until all pixels belong to some region. The key step of region growing is to model the similarity criterion which usually needs parameterization to avoid the leaking problem. The difference between the intensity of current pixel and neighbor pixels is generally used for similarity criterion, and the acceptable distance of the difference is set by user with constant. The seed point is necessary to region growing approach, and it is normally manually selected. This also could lead to different results from different observations. And a problem of region growing is leakage, since it is difficult to set a threshold value which confines an actual object.

2.1.2 Variational Methods

Variational methods are to determine the function that minimize (or maximize)

a functional. In general, there can be more than one independent variable and the integrand function can depend on several functions and their higher derivatives. In segmentation methods, they are based on energy functional where the optimum describes a good segmentation. To use variational methods, it is necessary for a curve to be defined. The curve defines the partitioning of the image and a lot of image derived terms in the energy function, such as image intensity, gradient, various feature, etc.

The energy functions are solutions of the Euler-Lagrange equations (i.e., variables are updated with infinitesimal steps) that are obtained by setting the first variational derivatives of the functional w.r.t. each function equal to zero. The segmentation of an image can be generated with an initial solution, such as a circle, a rectangle and random blobs. Variational methods may be categorized as either explicit or implicit by the representation of the curve and updated schemes.

The explicit formulation (parametric model) was proposed by Michael Kass et al. [56] with a deformable contour, known as snake. It is represented by explicit curve and it moves to an object boundary, pulled by external forces computed from the image. This framework attempts to minimize an energy associated to the current contour as a sum of an internal and external energy. The external energy is supposed to be minimal when the curve is at the object boundary position. The most straightforward approach consists in giving low values when the regularized

gradient around the contour position reaches its peak value. The internal energy is supposed to be minimal when the snake has a shape which is supposed to be relevant considering the shape of the sought object. The most straightforward approach grants high energy to elongated contours (elastic force) and to bended/high curvature contours (rigid force), considering the shape should be as regular and smooth as possible. The snake energy is defined as follows

$$E[C(s)]=-\int|\nabla I(C(s))|^2 ds+v_1\int|C'(s)|^2 ds+v_2\int|C'(s)|^2 ds \qquad (2.1)$$

where C(s) is a parametric curve with parameter s, I is the image, and C′ and C″ are the first and second derivatives of C with respect to its parameter s. These forces contain high-level information, such as contour curvature and low level information, such as image gradient direction.

The active contour model was the starting point for image segmentation using variational method. However, it suffers from some drawbacks. The main drawback is the explicit curve representation which does not naturally handle topological changes (i.e. the snake cannot split and merge). To allow the changes, it requires complex reparameterization algorithms. In addition, since the nodes of the curve are affected by local image features, the solutions tend to be very sensitive to a proper initialization and it is easy to fall into the local minima. Also, from a

mathematical point of view, the energy function is not intrinsic since it depends on the parameterization of the curve. This means that the energy will change if the parameterization changes, which clearly is an undesirable property.

The implicit formulation (geometric model, level set) is proposed by Osher and Sethian [57], apply segmentation problem into level set function which has a higher dimension by evolving a surface instead of a contour. Let *C(p)* be a closed planar curve in explicit representation and *C(p, t)* be an evolving curve toward normal vector N at time t. The speed of this propagation is supposed to be a scalar function of the curve the curvature K.

$$\left\{\begin{array}{l}\dfrac{\partial C}{\partial t}(p)=F(K)N\\ C(p,0)=C_0(p)\end{array}\right\} \qquad (2.2)$$

An Euler-Lagrangian approach can be used for producing the curve equation of propagation in order to execute the curve propagation for the position of the curve. The position of the curve is changed by difference approximation scheme. The one of the drawbacks from this approach is not capable to deal with topological changes. In order to solve this problem, the curve should detect and deal with merging and splitting the point of the curve. However, it is very hard to implement this approach and there are not very suitable numerical approximation schemes for

this curve representation. To solve this problem, level set is proposed which is visualized in figure 2.1

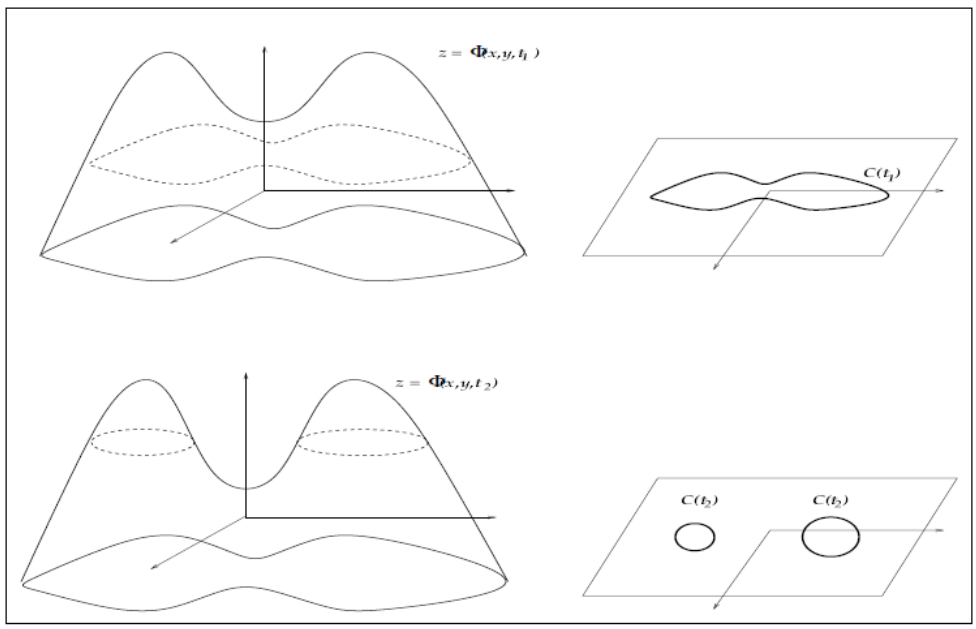

Figure 2.1 The concept of level set and curve evolution [58]. The left shows the evolving level set function, and the right shows the curve corresponding to the zero level set values. This method allows the change of object topology.

Let $\varphi(x, y, t) : R^2 \times [0, T] \rightarrow R$ be an implicit representation of the curve $C(p, t)$ and the position of the curve at t is represented the position of the zero level set.

$$\begin{Bmatrix} C(p,0)=\{(x,y):\varphi(x,y,0)=0\} \\ C(p,t)=\{(x,y):\varphi(x,y,t)=0\}, C(t)=\varphi^{-1}(0) \end{Bmatrix} \qquad (2.3)$$

where *C(p, 0)* is the initial curve (i.e. time t = 0). The problem is how to evolve the curve (level set function, φ) and how to solve this evolution in time. Let φ_t be the partial derivative of φ w.r.t. the time for the curve points, and it is given by the chain rule as follows.

$$\varphi(C(t),t)=0 \quad \Rightarrow \quad \frac{\partial \varphi}{\partial C}\cdot\frac{\partial C}{\partial t} + \frac{\partial \varphi}{\partial t} = 0 \qquad (2.4)$$

As described earlier, $\frac{\partial C}{\partial t}(p)=F(K)N$, $\frac{\partial \varphi}{\partial C}=\nabla\varphi$ and $C_t = FN$ the final motion equation for φ is as follows.

$$\varphi_t+\nabla\varphi C_t=\varphi_t+\nabla\varphi FN=\varphi_t+F\nabla\varphi\frac{\nabla\varphi}{|\nabla\varphi|}=\varphi_t+F|\nabla\varphi|=0 \qquad (2.5)$$

This last equation defined the motion of φ. Given φ at time t = 0, and its motion over time, it is now possible to know *φ(x, y, t)* at any time t by evolving the initial *φ(x, y, t=0)* over time (see figure 2.2). This equation refers to Eulerian formulation for the curve evolution and is a Hamilton-Jacobi type of equation.

In order to propagate smoothly, the curvature values can be used directly to the level set function.

$$\kappa = \nabla \frac{\nabla \varphi}{|\nabla \varphi|} = \frac{\varphi_{xx} {\varphi^2}_y - 2\varphi_{xy} \varphi_x \varphi_y + \varphi_{yy} {\varphi^2}_x}{({\varphi^2}_x + {\varphi^2}_y)^{\frac{3}{2}}} \qquad (2.6)$$

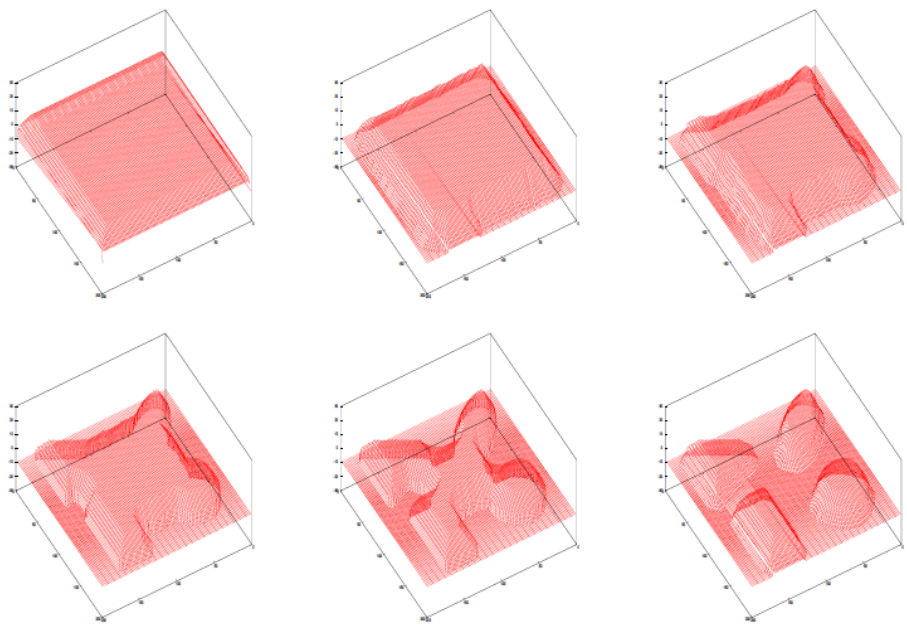

Figure 2.2 Level set and curve propagation. The evolution of the level set function at time t. As time passes, the curve of level set function evolves smoothly.

2.1.3 Image Features of the Curve

Although the deformable model of the explicit and the implicit curve differ in formulation, they generally use edge information (i.e. image gradient) or similarity of region information (i.e. image intensity) for the image segmentation. In explicit models, a typical formulation for the external energy [56] is given by

$$E_{ext}(C) = -\int_0^1 \left|\nabla I(C(s))\right|^2 ds \qquad (2.7)$$

This energy term uses edge information from the magnitude of the image gradient. C represents the explicit curve model by curve length s, ∇I is the image gradient along the curve. When the image gradient is maximum, the external energy term is minimized, which means that the explicit model is attracted by strong edges that correspond to pixels with local maximum image gradient values. On the other hands, the energy function of the implicit model for driving the curve is as follows.

$$E(C) = \int_0^1 g(\left|\nabla I(C(s))\right|)\left|C'(s)\right| ds, \quad where\ g(\left|\nabla I\right|) = \frac{1}{1+\left|\nabla I\right|^2} \qquad (2.8)$$

This energy term uses the curve of level set function with the image gradient information. To minimize the energy function, the curve deforms along its normal direction and its speed is controlled by the speed function g which is composed of the edge information. The speed function depends on image gradient and it is positive in homogeneous areas and zero at ideal edges. Therefore, the curve moves at a velocity proportional to its curvature in homogeneous regions and stops at the edges.

Although the image gradient information is used in both the explicit and the implicit model, this edge information is sensitive to noise and easy to stuck in local minimum. In the explicit model, it can leak through boundary gaps or create some holes or blobs. To solve these problems, there has researched the method to use not

only edge information but also region information in the curve models.

One of those methods is to augment the explicit model. Assuming that the image has the partition of the image into an object region and a background region, a region-based energy term for active contours is introduced in [59], which includes external energy term defined on the two regions, foreground and background. In [60], a generalized energy function that combines balloon force and region growing is presented and the energy minimization is guaranteed to converge to a local minimum. However, this formulation still does not solve the problem of unifying shape and appearance, due to the large difference in representation for shape and appearance. The model shape is represented using an explicit curve, the region intensity statistics are assumed by parameters of a Gaussian distribution. In other hybrid segmentation frameworks, a region based module is used to get a rough binary mask of the object of interest. Then this rough boundary estimation serves as initialization for a deformable model, which will deform to fit edge features in the image using gradient information.

Along the curve of implicit models, the region information has been mostly based on solving reduced cases of the minimal partition problem in the Mumford and Shah model for image segmentation [61]. The Mumford-Shah model is based on an optimal piecewise smooth function and pursued to approximate an observed image, such that the function varies smoothly and rapidly within each region across

the boundaries of different regions. The solution represents a partition of the image into several regions. The energy function of the Mumford-Shah model is given by

$$F^{MS}(u,C)=\int_{\Omega}(u-u_0)2dxdy+a\int_{\Omega/C}|\nabla u|^2dxdy+b|C| \qquad (2.9)$$

where u_0 is the observed image, u is the optimal piecewise smooth approximation of u_0 which we intend to obtain. Ω is the image domain, ∇u is the gradient of u, and C is the curve that approximate the edges in u_0. The first term of the F function minimizes the difference between u and u_0, the second term represents the smoothness of each region, and the third term constraints the boundary curves C to be smooth and represents the shortest distance.

Although the Mumford-Shah model incorporates gradient and region criteria into a single energy function, no practical globally-optimal solution for the function is available. Besides the gradient information of this model is only used for smoothness, not for detecting boundary. In the recent few years, progress has been made and solutions for several reduced cases of the Mumford-Shah functional have been proposed in the level set framework. Yezzi et al. [62] proposed the method which is able to extract the regions of the image by mean intensity and variance.

Geodesic Active Region [58] is another method based on region information in a level set framework. The algorithm consists of two stages, modeling stage and segmentation stage. The modeling stage constructs a likelihood map of edge pixels and approximates region/class statistics using Gaussian mixture model. The

segmentation stage uses level set techniques to solve for a set of smooth curves that are attracted to edge pixels and partition regions to be expected properties of the associated classes. In summary of the above approaches, they all solve the frame partition problem and are computationally expensive when dealing with images that contain many objects.

2.1.4 Combinatorial Methods

The previous section described variational methods which approach where the image domain is regarded as continuous and segmentation was posed as an optimization in a continuous space. Several problems of computer vision and graphics can be formulated to minimize the energy function in the discrete field, which is considered to be a task of fundamental importance. However, the resulting optimization problems are very challenging, especially in the discrete field since many random fields exhibit a highly non-convex energy function that is NP-hard to optimize exactly. In addition, a difficulty comes from the fact that the discrete fields encountered in practice are typically of very large scale, which further implies that computational efficiency should be very seriously considered. In this section, we describe combinatorial methods formulated as a discrete optimization problem on the pixels of the image and the main directions in this area for

completeness. And we present the review of optimality, dynamic programing and a wide range of state-of-the-art discrete optimization algorithms, i.e. graph-cut method.

Optimality of solutions: As described earlier, the variational methods previously presented use image gradient and gradient descent or stochastic gradient descent search for optimization which can be guaranteed to find stationary points, which means extremes. In many cases, it is not known whether the solution found is a local minimum, maximum or a saddle point among the extremes. Furthermore, the solution depends on the initial condition (the position and shape of the curve for image segmentation), which means that good initial condition provides good results. The main benefit of the combinatorial methods is that a global solution (or at least strong local solution) can be guaranteed as far as the objective function satisfies some conditions. This has several advantages: First, the solution is not depending on a good initial condition due to the guarantee of strong local solution, so the initial curve can be placed arbitrarily and be any shapes in the image. Second, the quality of the solution relates directly to the energy functional and the parameters controlling the functional, rather than the initialization or other numerical implications of the implementation. Some applications might benefit from the possibility of inducing a local optimum by a controlled initialization, such

as extracting a particular branch of a blood vessel tree. However, In general, combinatorial methods can be considered more robust because of the guaranteed global solution.

Dynamic programming and optimal paths: As the snake algorithm in variational methods, the combinatorial methods for segmentation begin with explicit (parametric) representations of object boundaries. Amini et al. [63] presented dynamic programming for finding a global optimum of the Snakes energy for the first time. Other researchers have proposed similar techniques based on dynamic programming to find optimal paths [64-66]. However, these approaches are limited to 2D images since the properties of 3D geometry require fundamentally different explicit representations.

Graph cuts: A number of the problems that increase in computer vision and image processing can be naturally expressed in terms of energy minimization. For example, many problems of computer vision attempt to assign labels (such as intensity, disparity, segmentation regions) to pixels. In the presence of these uncertainties, finding the best label in the image can be regarded as an optimization problem. Minimum cut (maximum flow) algorithms have emerged as an elegant and increasingly useful tool for exact or approximate energy minimization in the

last few years. This method is to construct a specialized graph for the energy function to be minimized such that the minimum cut on the graph also minimizes the energy (either globally or locally). The minimum cut can be computed very efficiently by max flow algorithms. These methods have been successfully used for a wide variety of vision problems, especially image segmentation. An important contribution for segmentation based on graph cuts was presented by Boykov and Jolly [67, 68]. In this work, pixels are classified as being either inside or outside the object, making this a combinatorial method using a discrete representation. Thus, compared to the previously outlined path-based approaches, this method generalizes to higher dimensions more easily. The success of the method relies on an efficient minimum cut algorithm which computes a globally optimal cut (see figure 2.3).

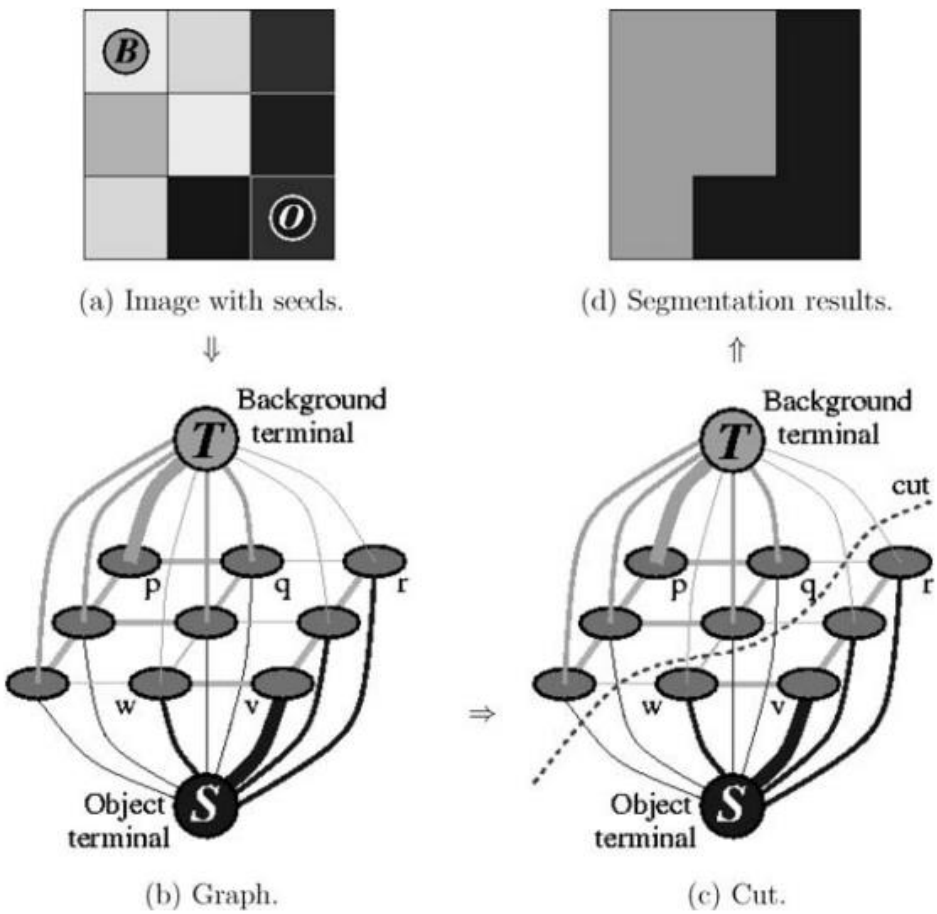

Figure 2.3 An example of image labelling for a simple 2D segmentation example in a 3×3 image. The seeds are O = {v} and B = {p}. The weight of each edge is represented by the edge's thickness. The boundary term defines the costs of n-links while the regional term defines the costs of t-links. The edges of n-link which have low weight (cost) are selected for the minimum cost cut. Seeds are implemented via infinity cost for t-links. This can be computed efficiently in low-order polynomial time using max-flow/min-cut algorithms on graphs [68]

2.1.5 Difficulty of Segmentation

It is difficult to segment specific organ from the medical image. There are several reasons to be difficult to extract interested regions [69].

Partial volume effects: Partial volume effects are artifacts that occur where multiple tissue types contribute to a single pixel, resulting in a blurring of intensity across boundaries. Figure 2.4 shows how the partial volume effects is generated, leading to ambiguities in structural definitions. Figure 2(a) shows the ideal image which is no partial volume, and figure 2(b) shows the acquired image with partial volume. It is difficult to precisely determine the boundaries of the two objects in partial volume effects. They are common in medical images, particularly for 3-D CT and MRI data, in which the resolution is not isotropic and is quite poor along one axis of the image.

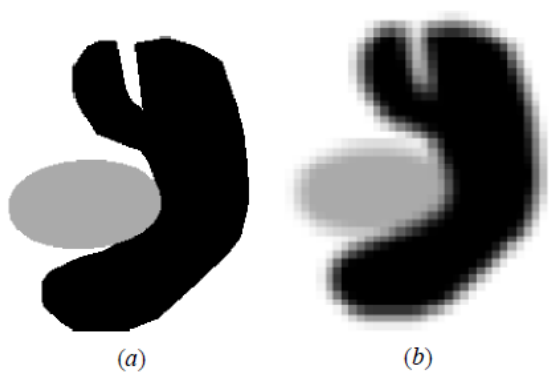

Figure 2.4 Illustration of partial volume effect [69]. (a) Ideal image. (b) Acquired image.

Intensity inhomogeneity: The one of the segmentation difficulty is intensity inhomogeneity artifact [69] which causes a shading effect to appear over the image. This artifact can significantly degrade the consistent of the intensity value over the image. Although scanner technology has improved and several approaches have been proposed in the literature for performing tissue classification in the presence of intensity inhomogeneity, it still remains. Figure 2.5 shows an axially acquired MR cardiac image with a myocardial infarction. Figure 2.5(a) shows the original MRI image, 2.5(b) shows the estimated gain field, 2.5(c) shows the result of the segmentation for three classes, and 2.5(d-f) shows the probability of the segmentation for three classes. Intensity inhomogeneity is noticeable particularly near the breasts.

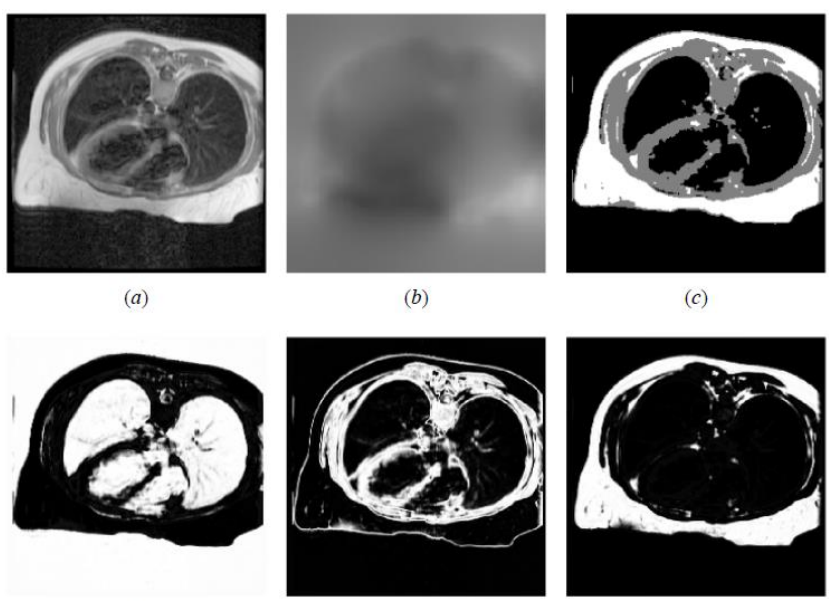

Figure 2.5 An example of intensity inhomogeneity and soft segmentation [69]. (a) Magnetic resonance heart image. (b) Estimated gain field. (c) Hard segmentation into three classes. (d–f) Probability of the three classes.

Weak or no edge/boundary: The other reason is that the object might have weak or no edge and boundary (see figure 2.6). The blue ellipse of figure 2.6 describes storing edge, so this is very easy to segment. But the red ellipse of figure 2.6, we cannot find any edge or boundary. That is very difficult to segment each chamber, such as atrium and ventricle because this cardiac CT image has very weak edge. So it is difficult to segment in this edge.

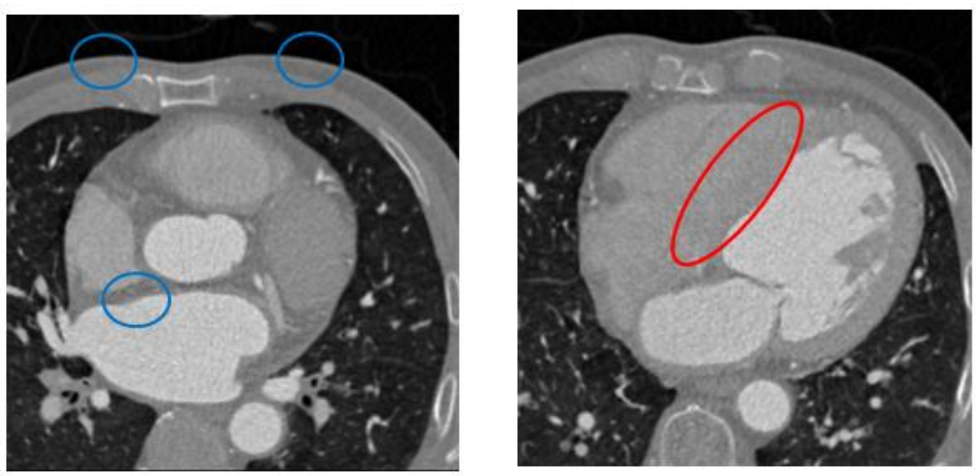

Figure 2.6 A cardiac CT image with strong edge and weak edge. The blue ellipses represent strong edge between airway and heart, and the red ellipse represents weak edge between right ventricle and left myocardium.

2.2 Heart Segmentation

As described earlier, it is hard to extract heart region from CTA for several reasons. First, the shape and topology of the heart is very complex. Second, the heart is an organ to be imaged because of its characteristic. Third, the heart can be occluded by other organ or tissue such as fat, liver or the chest wall. For these reasons, the heart has been usually extracted using model-based methods, with statistical or non-statistical model. They are segmentation methods which are based on a standard mean shape of the heart, or user defined landmarks in the image. Model-based techniques yield more robust algorithms and they are capable of working well on various images. However, the more robust the algorithm is, the more details will be lost in the segmentation process. Besides, it is necessary of template model and huge training data.

To the best of our knowledge, there are very few attempts to segment the heart, especially four chambers, not using model-based method. All of those attempts required careful manual initial condition positioning. The one of the main model-based cardiac segmentation methods is active shape models.

2.2.1 Non-Model-Based Segmentation

The heart segmentation using non-model-based method has rarely researched. To our knowledge, there is one method using Chan-Vese algorithm [30]. The iterative Chan-Vese algorithm is proposed for whole heart segmentation [29]. The goal of this study is to extract the heart muscle from high resolution cardiac CTA of the thorax and to produce 3D meshes that is adequate for numerical simulation of the heart.

The Chan-Vese model was derived by Mumford-Shah energy model. The level set formulation of the Chan-Vese model is as follows.

$$E_{CV}(\phi, c_1, c_2) = \int_{\Omega} (g - c_1)^2 (1 - H(\phi)) dx + \int_{\Omega} (g - c_2)^2 H(\phi) dx + \int_{\Omega} |DH(\phi)| dx \tag{2.10}$$

where H(•) is Heaviside function and DH(•) is the derivative of H(•). Olivier et al. [29] used an L^1 fidelity term for the computational efficiency instead of L^2 fidelity and iterative scheme.

$$E_{ICV}(\phi, c_1, c_2) = \int_{\Omega} |g - c_1| (1 - H(\phi)) dx + \int_{\Omega} |g - c_2| H(\phi) dx + \int_{\Omega} |DH(\phi)| dx \tag{2.11}$$

This method segmented only the whole heart, not each chamber (see figure 2.7)

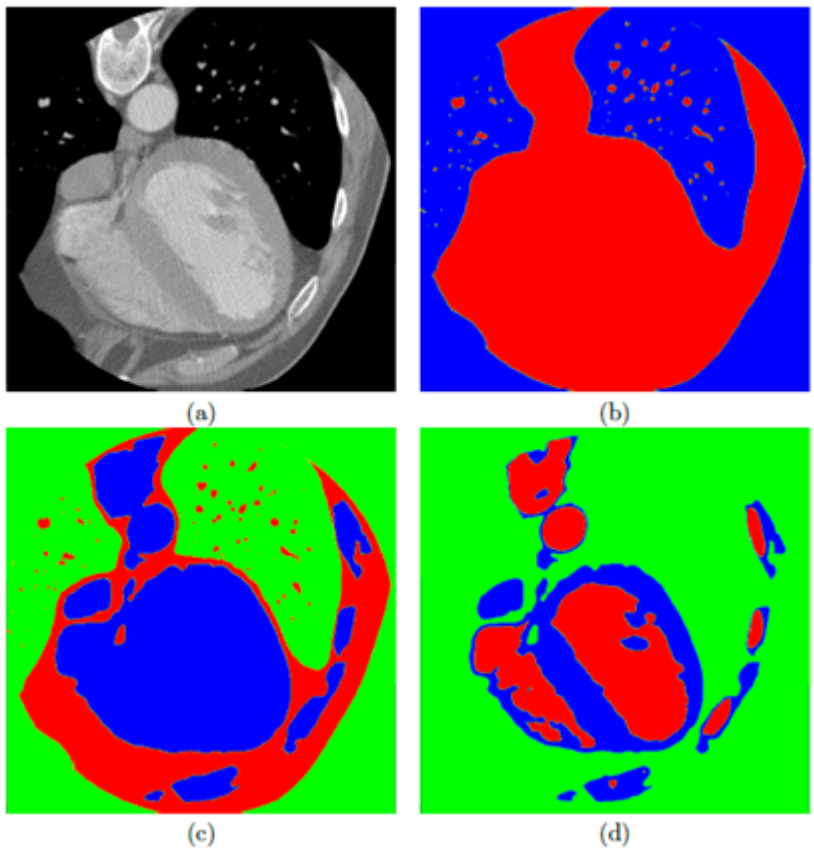

Figure 2.7 2D iterative segmentation of the heart in the cardiac CTA. (a) An original image (b) the result to be applied first Chan-Vese model. (c) The result to be applied second Chan-Vese model only the red region of the (b). (d) The result to be applied third Chan-Vese model only the blue region of the (c).

2.2.2 Unstatistical Model-Based Segmentation

Unstatistical model-based segmentation is similar as active contour model [56], except the one thing that a template model is necessary to segmentation. Their

original idea is to start with a parametric curve in 2D (a surface in 3D) and to let the curve evolve until it stops on the boundary of the object. To evolve toward the boundary exactly, the template mesh is deformed by minimizing the sum of the quadratic distances between the triangle centers and the boundary point [70].

$$E_{external} = \sum_{i=1}^{T} \omega i \left(\frac{\nabla I(x_i^{target})}{\left\| \nabla I(x_i^{target}) \right\|} \cdot (x_i^{target} - c_i) \right)^2 \qquad (2.12)$$

where c_i is the center of the triangle, x_i^{target} is the detected boundary points. The term , $x_i^{target} - c_i$ is projected onto the direction of the image intensity gradient at the target point. This makes the external energy invariant to movements of the triangle within the object tangent plane, preventing the triangle from becoming stuck at the target position. Minimizing only this term can lead to irregular shapes due to some false target points and mission boundaries. In order to avoid this problem, prior shape knowledge was used by internal energy term.

$$E_{internal} = \sum_{i=1}^{V} \sum_{j \in N(i)} \left((v_i - v_j) - (T[m_i] - T[m_j]) \right)^2 \qquad (2.13)$$

To constraint the deformation it is required that the vertices should stay close to the reference shape (mean shape). The objective function to minimize is given by $E = E_{external} + \alpha E_{internal}$. Figure 2.8 shows the template mesh model and the result of the heart segmentation using unstatistical deformable model.

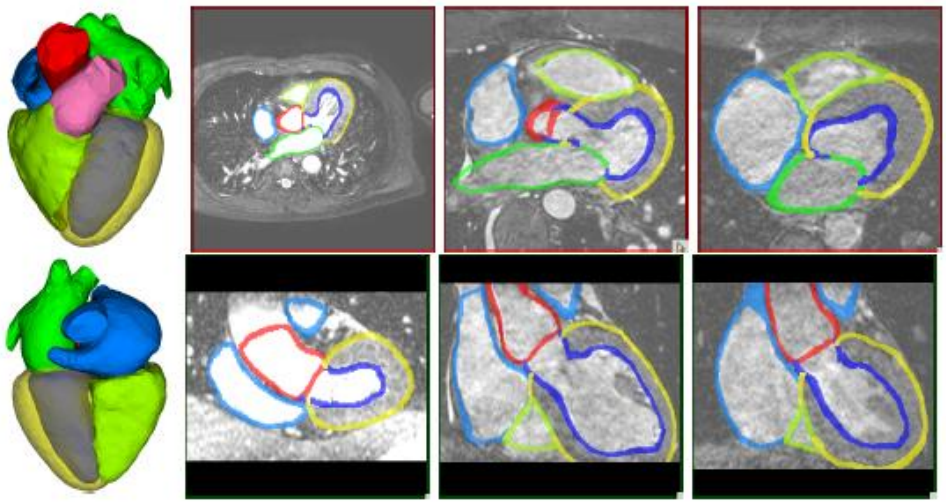

(a) (b)

Figure 2.8 The template model of the heart and the result of the heart segmentation using unstatistical model-based method. (a) The template model (mean shape model) (b) The result of the heart and each chamber.

2.2.3 Statistical Model-Based Segmentation

A model-based method became available with the development of statistical shape models, capable of capturing statistical shape and gray level information from sets of training data. Statistical shape modeling has proven to be one of the most influential developments in knowledge-driven image analysis in the last decade. The most popular method based on statistical model is ASM [17]. This model is proposed in 1995, very classic method, but it is used broadly until now

and it becomes basis of the other model-based methods. It is necessary of trained from sets of examples and match the model to image iteratively. This method is composed of two stages: train model and boundary detection.

The train model step is organized as three steps, labeling, alignment and principle component analysis. In the labeling step, the feature of the object on training data is labeled manually. The point distribution model is an approach for representing the mean geometry of a shape and some statistical modes of geometric variation inferred from a training set of shapes. Active shape model is the most popular method of point distribution model (see figure 2.9).

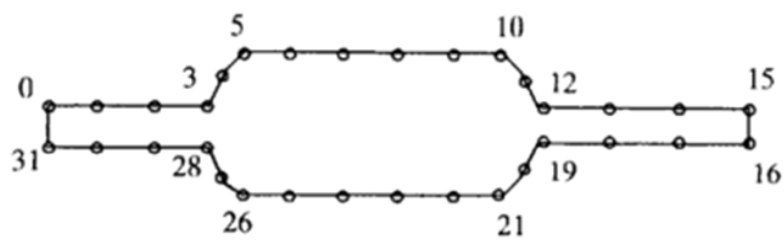

Figure 2.9 The labeling step of the train model stage. Each feature of the object is labeled manually.

In the alignment step, the landmark of the features is aligned. In other words, all labeled train model has the same center, scale and orientation. Principal component analysis (PCA) is then performed to get the main directions of shape variability on the aligned shapes. The aligned set of shapes is transformed onto a

basis of eigenvectors describing the shape variation in the training set. The eigenvectors are calculated by applying the PCA on the covariance matrix of the training set. A point in the eigenspace is a linear combination of eigenvectors representing a particular shape, while the origin in the eigenspace corresponds with the average shape from the training set. Synthesized shape from the model can be written as

$$X = \overline{X} + \Phi b \qquad (2.14)$$

where $\overline{X}$ is the mean shape, Φ is a matrix containing the m-eigenvectors and b is a m-dimensional parameter vector. As b changes, it is possible to control the deformation of the model X.

In the boundary detection step, shape model is matched to new image, from template mesh model to the boundary of the object. This step is local optimization, and the best matching point on the object is searched along profiles by updating parameters b.

Most of the model-based segmentation of the heart has used the ASM in 3D. The one of the main approach using statistical model-based segmentation is proposed in 2008 [24]. This method is similar as ASM, only difference between this model and classic ASM is to use the heart model. The point distribution model for heart is expressed as follows.

$$m = \bar{m} + \sum_{m=1}^{M} P_m \Phi_m \qquad (2.15)$$

where $\bar{m}$ is the mean heart shape of the training set, Φ_m are the first M eigenmodes with largest variance, and P_m is the corresponding weight. This equation is similar as the equation of the ASM, (2.14). Figure 2.10 shows that the result of the heart segmentation using statistical model-based method.

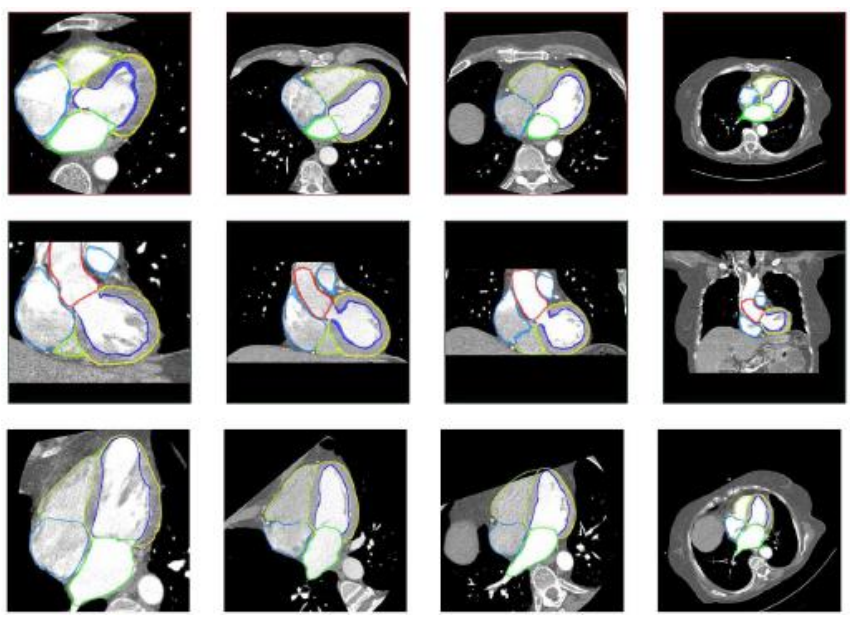

Figure 2.10 The results of the heart segmentation using statistical model-based method. First row shows the cases in axial view corresponding to the slices reconstructed by the scanner. Second row is a coronal view of the data. Third row shows four-chamber view of the data.

Chapter 3. Gradient-assisted Localized Active Contour Model

3.1 Localized Active Contour Model (LACM)

As described earlier, ACM has become the one of the most popular in recent years for segmentation. The basic idea is to evolve the curve by deforming to minimize the energy functional for the segmentation of the specific organ. In this chapter, we review the frame work of the original LACM [31] that allows any region-based active contour segmentation method to be re-formulated so that it relies on information from local image regions. And we proposed GLACM which is the improved method of the original LACM.

Active contours by local formulation are capable of segmenting objects with heterogeneous feature profiles that would be difficult to capture correctly using standard global methods (see figure3.1). Edge-based active contour models which utilize image gradients are very sensitive to image noise and dependent on the position of the initial curve because of its localizing characteristic. However, figure 3.1 shows that the edge-based algorithm is rather than region-based algorithm when the foreground and background are heterogeneous and share nearly the same

statistical models. To solve this problem, the local formulation is necessary to the ACM using region-based energy term.

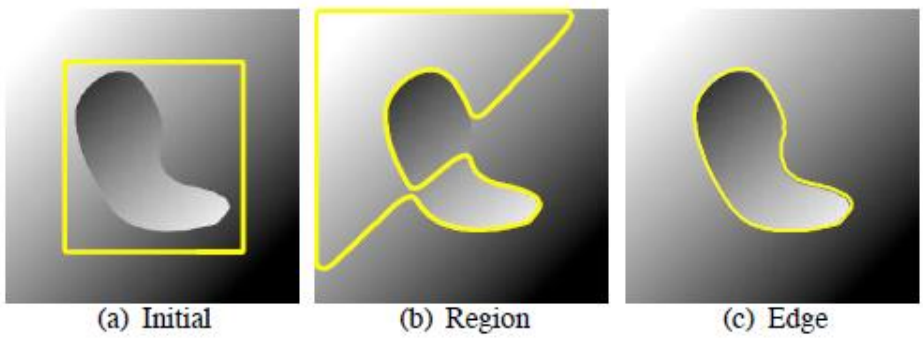

Figure 3.1 A synthetic image of a blob with heterogeneous intensity on a similar background. (a) Initial contour. (b) Unsuccessful result of region-based segmentation. (c) Successful result of edge-based segmentation.

Let *I* denote a given image, and let *C* be a closed contour represented as the zero level set of a signed distance function *Φ*. The interior of C is specified by the smoothed Heaviside function *H Φ*(x), and the exterior of C is defined (1-*H Φ*(x)).

$$H\phi(x)=\begin{cases}1, & \phi(x)<-\varepsilon \\ 0, & \phi(x)>\varepsilon \\ 1/2\left(1+\phi/\varepsilon+1/\pi\sin(\pi\phi(x)/\varepsilon)\right), & otherwise\end{cases} \tag{3.1}$$

To specify the area around the curve (i.e. narrowband), the smoothed Dirac delta function, the derivative of Heaviside function, is used.

$$\delta\phi(x)=\begin{cases}1, & \phi(x)=0\\ 0, & |\phi(x)|<\varepsilon\\ 1/2\varepsilon\left(1+\cos(\pi\phi(x)/\varepsilon)\right), & otherwise\end{cases} \tag{3.2}$$

The energy functional of the LACM is defined as follows, using characteristic function B and force function F.

$$B(x,y)=\begin{cases}1, & \|x-y\|<r\\ 0, & otherwise\end{cases} \tag{3.3}$$

$$E(\phi)=\int_{\Omega}\delta\phi(x)\int_{\Omega}B(x,y)\cdot F(I(y),\phi(y))dxdy \tag{3.4}$$

The characteristic function B decides the ranges of interested region in localized region (see figure 3.2).

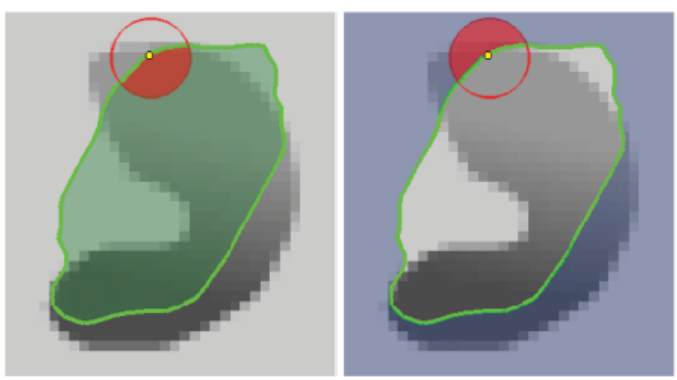

(a) Local Interior (b) Local Exterior

Figure 3.2 A ball is represented at each point along the evolving curve. This ball is split by the curve into local interior and exterior regions. The characteristic function B(x, y) neighborhood is represented by the larger red circle. In (a), the local interior is the part of

the red circle and in (b), the local exterior is the part of the red circle.

In computing the energy functional E, it is only considered near the contour and the inhomogeneity is ignored where is far away. In order to keep the curve smooth, the internal energy term is usually used, and it is added to the LACM energy functional to penalize the arc length of the curve.

$$E(\phi)=\int_{\Omega}\delta\phi(x)\int_{\Omega}B(x,y)\cdot F(I(y),\phi(y))dxdy + \lambda\int_{\Omega}\delta\phi(x)\|\nabla\phi(x)\|dx \tag{3.5}$$

By taking the first variation of this energy w.r.t. Φ, the evolution equation of the level set function is as follows.

$$\frac{\partial\phi}{\partial t}(x)=\delta\phi(x)\int_{\Omega}B(x,y)\cdot\nabla\phi(y)F(I(y),\phi(y))dy + \lambda\delta\phi(x)\,div\frac{\nabla\phi(y)}{|\nabla\phi(y)|} \tag{3.6}$$

Notice that the only restriction on the force function, F is that its first variation w.r.t. Φ can be computed. This ensures that most of all the force function of the region-based segmentation can be put into this framework.

There are several energy functions to be applied to this framework including uniform modeling energy. One of the most popular energy is the Chan-Vese model which is a piecewise-constant intensity model. The uniform modeling energy is

used in this study, which is similar to the Chan-Vese model.

$$E_{UM}(\phi)=\int_{\Omega}\left[H\phi(x,y)(I(x,y)-u)^2+(1-H\phi(x,y)(I(x,y)-v)^2\right]dxdy \quad (3.7)$$

$$u=\frac{\int_{\Omega} H\phi(x,y)\cdot I(x,y)dxdy}{\int_{\Omega} H\phi(x,y)dxdy},$$
$$v=\frac{\int_{\Omega}(1-H\phi(x,y))\cdot I(x,y)dxdy}{\int_{\Omega}(1-H\phi(x,y))dxdy} \quad (3.8)$$

where u and v are the interior and exterior regions of local mean intensities. This energy models the foreground and background as constant intensities represented by u and v. The corresponding local energy *F* is formed by replacing u and v.

$$F_{UM}=H\phi(x,y)(I(x,y)-u)^2+(1-H\phi(x,y)(I(x,y)-v)^2 \quad (3.9)$$

This F can be used to the localized energy function. In order to get the evolution equation for Φ, the derivative of F w.r.t. Φ is used. The evolution equation of the localized uniform modeling energy function is as follows.

$$\frac{\partial\phi}{\partial t}(x)=\delta\phi(x)\int_{\Omega}B(x,y)\delta\phi(x)\cdot((I(y)-u)^2-(I(y)-v)^2)dy + \lambda\delta\phi(x)\,div\left(\frac{\nabla\phi(y)}{|\nabla\phi(y)|}\right) \quad (3.10)$$

This uniform modeling equation finds its minimum energy when the interior and

exterior are best approximated to u and v. In the localized framework, the minimum is obtained when each point on the curve has moved such that the local interior and exterior about every point along the curve is best approximated by local means. Figure 3.3 shows the comparison with global image statics and local image statics on the cardiac CTA.

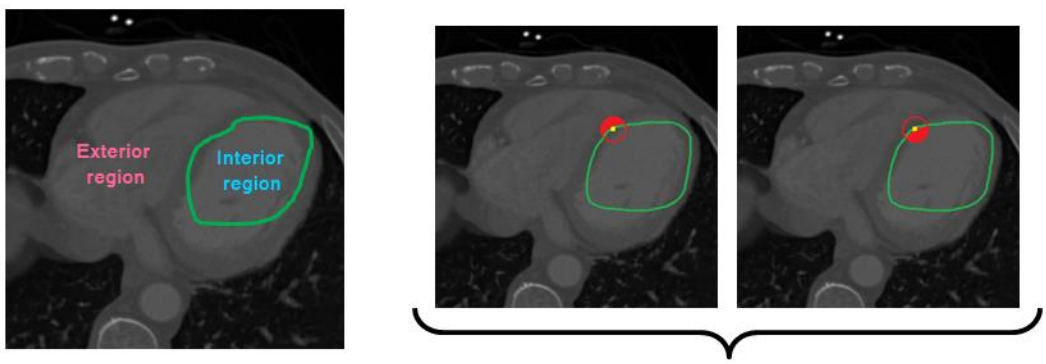

(a) (b)

Figure 3.3 The comparison with global image statics and local image statics on the cardiac CTA. (a) The interior region and exterior region of the global statics. (b) The localized interior (right) and exterior (left) region.

3.2 Gaussian-Pyramid Edge Map

As described in previous section, LACM uses the region information with localized formulation. Localized segmentation energies are useful for image segmentation, which may be difficult for existing global region-based segmentation

techniques. The ability of localized segmentation methods to capture objects with varying intensities makes them ideal for use in many medical imaging applications. However, it is not enough to segment the medical image which has many heterogeneous regions only using region-based information. In particular, in the case of heart segmentation, cardiac CT has many noises and heterogeneous regions. Besides, the edge information is the one of the most important data to decide the boundary of the object.

In this work, we improved the LACM by integrating the edge energy term to the origin approach. Since the edge information is highly localized image information, it has very small capture range, so it tends to stick to the local minimum. Classic edge map is generated by convolution of the Gaussian filter for only one sigma. This map is composed of the edge information in only one scale space. As described earlier this information is easy to fall on the local optimum and the range of the curve evolution is limited. To solve this problem, we proposed Gaussian-pyramid edge map which use the edge information in several scale spaces and is generated by accumulating the image gradient values for all scale spaces. Figure 3.4 shows the process of the generating Gaussian-pyramid edge map. When the CT images are loaded, the Gaussian pyramid of the images is generated. .This is a pyramid data structure with the edge map of multi-scale Gaussian-filtered images with different sigma values. A Gaussian-pyramid edge

map is generated by accumulating each Gaussian-derivative image with different sigma values.

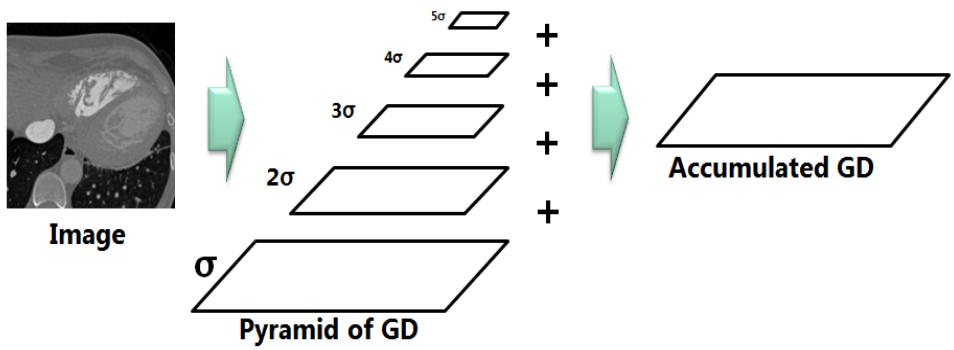

Figure 3.4 The process of the generating Gaussian-pyramid edge map. First, the CT images are loaded. Second, the Gaussian derivative pyramid is obtained from the multi-scale images. Finally, the Gaussian-pyramid edge map is generated by accumulating each Gaussian-derivative image.

This map is used to extract the left and the right heart region exactly, as described in Chapter 4. The equation of this map is as follows.

$$M_{GD}(I) = \sum_{i=0}^{n} W(i) \left| \nabla G_{\sigma} * I \right| \qquad (3.11)$$

M_{GD} is the Gaussian-pyramid edge map, * is the convolution operator, and $W(i)$ = i + 1. Figure 3.5 shows the comparison between the edge map for only one scale space and the Gaussian-pyramid edge map.

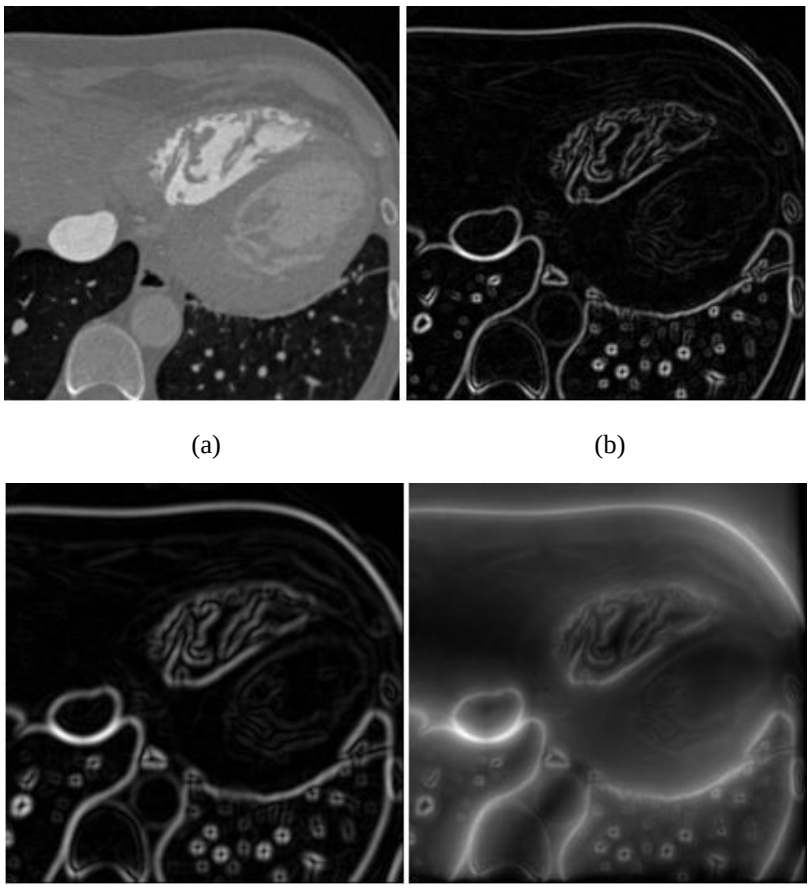

(a) (b)

(c) (d)

Figure 3.5 Gaussian-pyramid edge map that is the accumulation of the Gaussian derivatives with different sigma values. (a) Original CT image. (b) Gaussian derivative at $\sigma = 1.0$. (c) Gaussian derivative at $\sigma = 2.0$. (d) Final Gaussian pyramid edge map.

The edge map on a scale space, in figure 3.5(b) and (c), it has high value only around the edge. That is the reason why the edge-based methods have small capture range. On the other hand, the value of the edge map in the Gaussian pyramid is spread, so it increases the capture range of the curve evolution.

3.3 Adaptive Radius Function

As described in the section 3.1, the characteristic function *B*(x) is included in the LACM energy function, and it is a function in terms of a radius parameter r (see equation 3.3, 3.4 and figure 3.2). The circular region with a radius r is only considered at each point along the contour. This function will be '1' when point y is within a circle of radius r centered at x. Each point in the circular region is separated by the contour into the locally interior and exterior regions; accordingly, the radius affects the overall segmentation performance. Therefore, a larger local region is considered with a large radius for more accurate segmentation of the homogeneous region. However, the heterogeneous regions might not be correctly segmented with such a large radius. Conversely, it could be easily fallen into a local minimum with a smaller radius. To solve the problem of the constant radius in LACM, we propose an energy function in terms of an adaptively changed radius (see figure 3.6).

$$L(r) = \arg\max_{r} \left(\min \int_{\Gamma_x} \delta\Psi(\nabla I(x))\, dx \right) \quad s.t.\ 3 \le r \le R_{\max} \tag{3.12}$$

where R_{max} is the constant maximum radius and Γ is the normal vector of a contour bounded by the circle with radius r. R_{max} was experimentally determined as 9.

δΨ(x) is a modified Dirac delta function, defined as follows.

$$\delta\Psi(x)=\begin{cases}1, & |\Psi(x)|<const\\ 0, & otherwise\end{cases}, s.t.\ \Psi(x)=\frac{1}{x+\varepsilon} \tag{3.13}$$

By computing L(r), we obtain the maximum radius of the ball that minimizes the change of the gradient in the range of r. Figure 3.6 shows the comparison between the constant radius and variable radius of the characteristic function in the energy function.

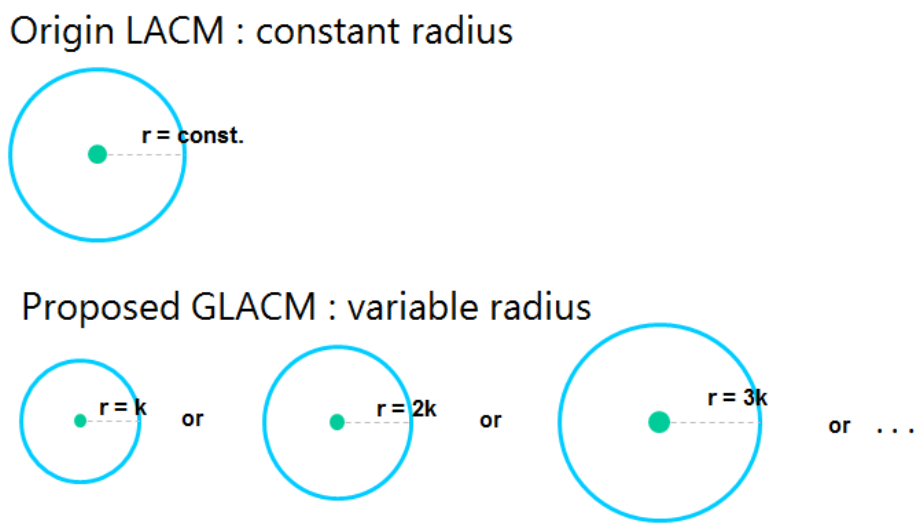

Figure 3.6 The concept of the adaptive radius function. The top image is the constant radius in origin LACM, and the bottom image is the variable radius in GLACM for characteristic function.

3.4 LACM with Gaussian-Pyramid Edge Map and Adaptive Radius function

In the section 3.1, 3.2 and 3.3, we reviewed the LACM and proposed the concept of the Gaussian-pyramid edge map and the adaptive radius function. In this section, we propose our proposed method, the GLACM. It considers not only region-based information but also edge-based information for a more accurate segmentation compared with a conventional LACM. For edge-base information, we used the Gaussian-pyramid edge map in order to increase the capture range of the curve evolution. And we used the adaptive radius function in order to prevent the curve to fall into wrong edge of undesired object. The proposed energy function of our GLACM is as follows.

$$E_{GLACM} = \int_{\Omega y} \left(\lambda (u - v)^2 + (1 - \lambda) g(M_{GD}(y)) \right) dy, \tag{3.14}$$

$$g(|\nabla u_0|) = \frac{1}{1 + |\nabla G_\sigma * u_0|^2}, \tag{3.15}$$

$$G_\sigma(x, y) = \frac{1}{2\pi\sigma^2} \exp\left(\frac{-(x^2 + y^2)}{2\sigma^2}\right), \tag{3.16}$$

where λ is a weight parameter, g is an edge indicator function, σ is standard deviation of Gaussian function, M_{GD} is the Gaussian-pyramid edge map (see

equation 3.11). The function, g(x), converges to 0 with $x \to \infty$, and 1 with $x \to 0$. Therefore, the edge indicator function has a low value near the edge.

Chapter 4. Segmentation of Four Chambers of Heart

4.1 Overview

The proposed method of four-chamber segmentation includes four main steps as shown in figure 4.1. First, we roughly segment the whole heart from the CTA. Second, the whole heart is separated into left and right sides. This is used for the seed volume in the subsequent step. Third, we expand these seed volumes, which are coarsely segmented in the first step in order to set an initial contour and segment accurate volumes of the left and right sides of the heart using our proposed GLACM method. Finally, the left and right sides of heart are separated into the atrium and ventricle.

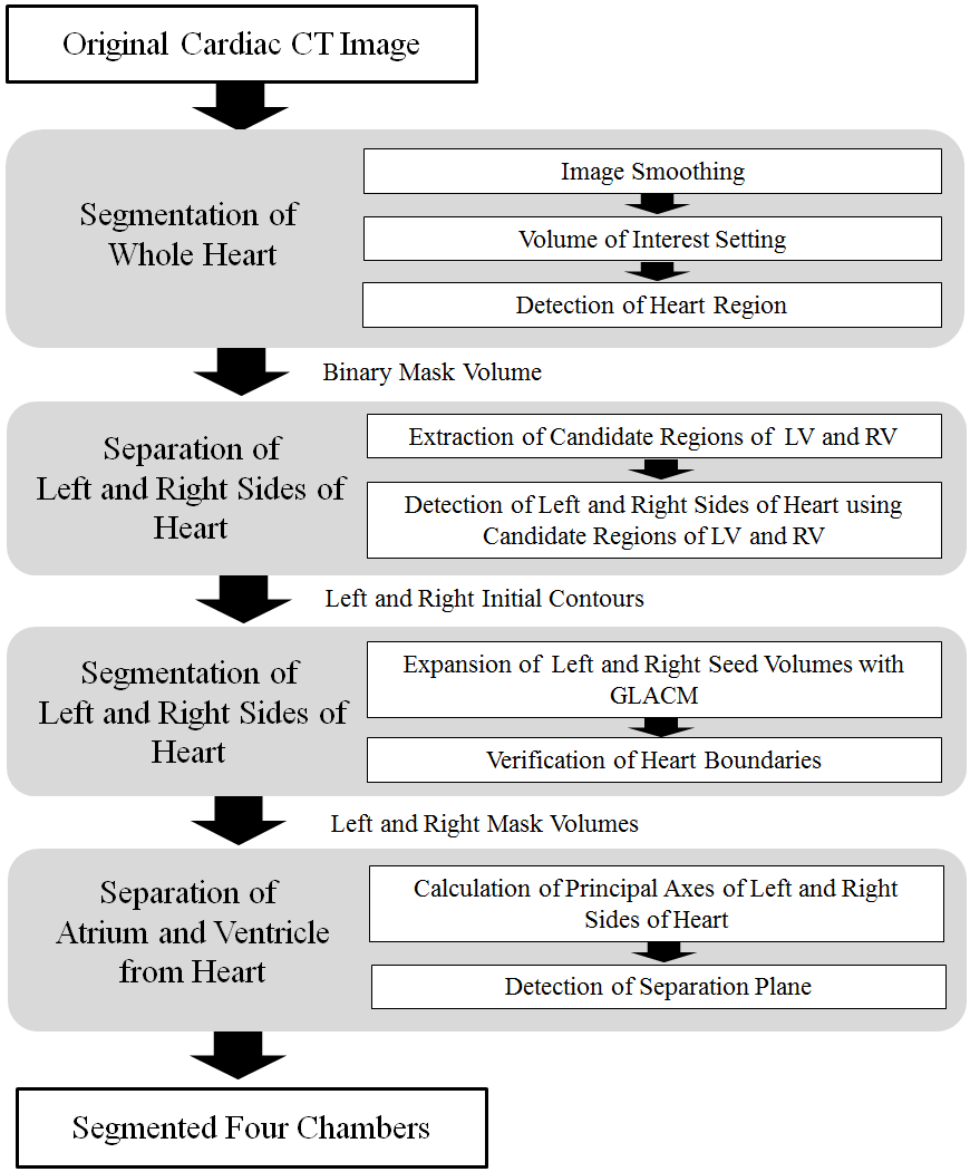

Figure 4.1 Process of four-chamber segmentation

4.2 Segmentation of Whole Heart

This step roughly segments the whole heart including the four chambers: left ventricle (LV), left atrium (LA), right ventricle (RV), and right atrium (RA). This whole heart is used to segment each chamber in the subsequent steps. In general, there is significant noise in the cardiac CTA and the boundaries of the four-chambers are ambiguous due to the inhomogeneous angiography (see figure 4.2).

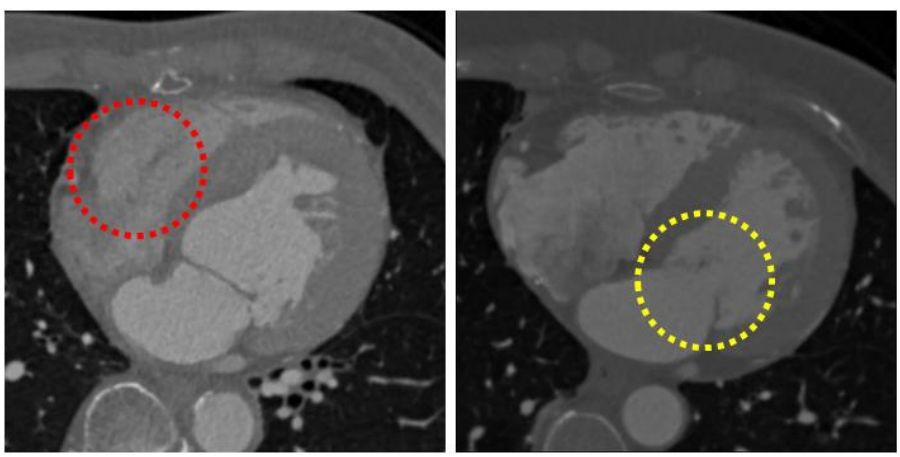

(a) (b)

Figure 4.2 Cardiac CTA. (a) Inhomogeneous region. (b) Ambiguous valve.

Therefore, it is difficult to segment the heart without appropriate preprocessing. A smoothing step would make the intensity distribution less variable by suppressing the noise. However, a simple smoothing blurs the heart

boundary. There are several image denoising methods. The one of the most popular image denoising method is an anisotropic diffusion filtering [32] in order to remove the noise but preserve the edge. However, this method is very computationally heavy one, we smoothed the images by applying the Gaussian filter and median filter (see figure 4.3).

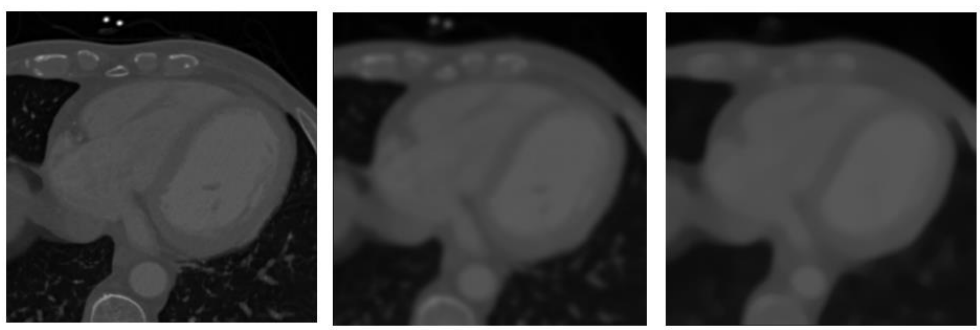

(a) (b) (c)

Figure 4.3 Image denoising. (a) Original image. (b) Gaussian filtered image. (c) Median filtered image.

For the heart segmentation, we initially segment the regions from these smoothed images using Otsu's thresholding method [33]. After the thresholding, the regions including the heart are detected and assigned a value of one. Other background regions are assigned a value of zero. However, although the heart region is detected, rib cages and lung vessels could be falsely included by this simple thresholding. Therefore, we label each structure using two-dimensional (2D) connected component labeling (CCL), slice by slice, to remove falsely

included regions (e.g., rib cages or lung vessels). Because rib cages and lung vessels appear as blobs or spots in the slice, they are eliminated by analyzing their areas (i.e., small components) and shapes (i.e., circular shapes) using 2D CCL.

Although rib cages and lung vessels are generally removed by the previous step, cardiac muscles outside the four chambers might still exist. To eliminate these, we apply k-means clustering [34] within the heart region (k = 15) and expand the chamber regions by comparing the mean CT value of each cluster (see figure 4.4).

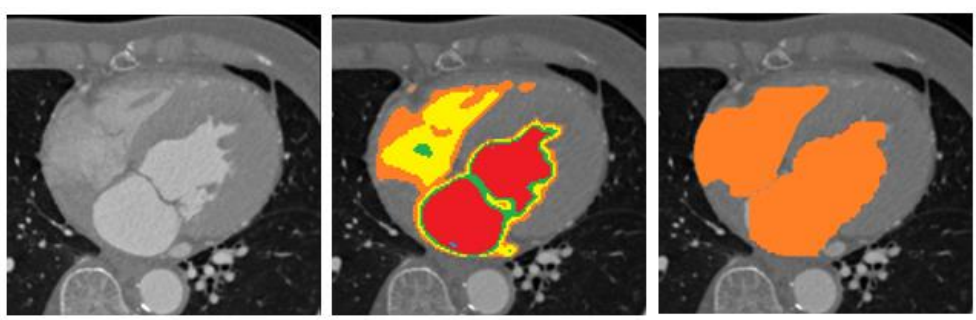

(a) (b) (c)

Figure 4.4 Result of k-means clustering. (a) Original image. (b) K-means clustering (k = 15). (c) Merging and removing clusters with respect to the intensity the cluster.

Each chamber generally has a higher CT value than the cardiac muscle. Therefore, the clusters, which have a lower mean intensity than the threshold value of 220 HU, are removed as cardiac muscles and the remaining clusters are

merged. The binary mask volume, obtained by the output of the k-means clustering, is used to extract the left and right sides of the heart volume in the subsequent step (see figure 4.5).

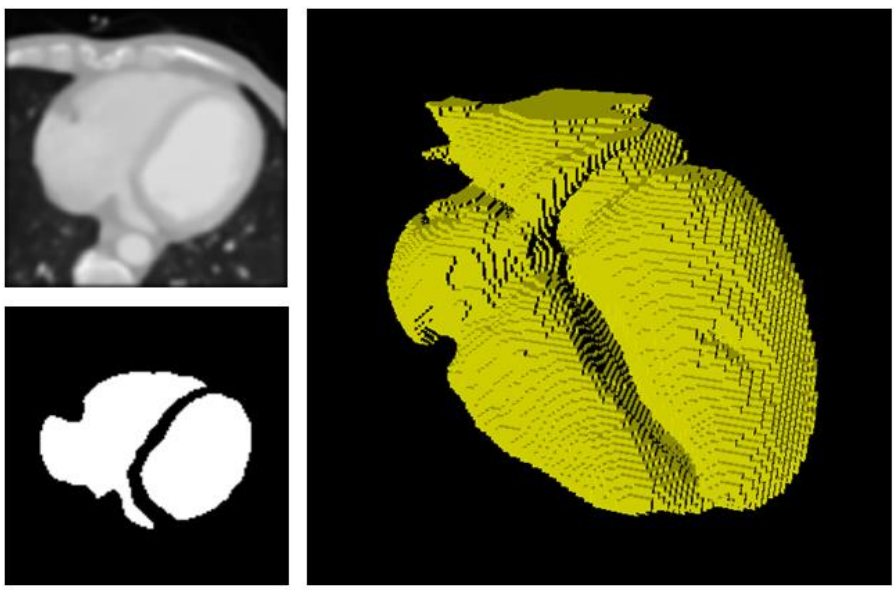

(a) (b)

Figure 4.5 Result of whole heart segmentation. (a) Top: filtered slice image; bottom: the region of k-means cluster. (b) 3D iso-surface rendering image of k-means cluster.

4.3 Separation of Left and Right Sides of Heart

In this step, we roughly split the whole heart into left and right sides. The left side of the heart consists of the LV and LA. The right side consists of the RV and

RA. Anatomically, the LV and RV are separately located in the lower slices whereas the LA and RA are not that easily distinguished in the upper slices due to the ambiguity in the boundaries between the left and right sides of heart. In this paper, we first extract the candidate regions of the LV and RV in the lower axial slices. Then, using the candidate regions of the LV and RV as seed volumes, we apply a power watershed [35]. This is a tool used to segment an object with weak boundaries for the separation of the left and right sides of the heart.

4.3.1 Extraction of Candidate Regions of LV and RV

Because there are only two components (i.e., LV and RV) in the lower axial slices, we can determine the LV and RV in the lower axial slices using 2D CCL, slice-by-slice, on the binary mask result of the whole heart acquired in the previous step. In the lower axial slices, the RV is generally located on the left side and the LV is located, relatively, on the right side. The center of the RV is usually located on the left-upper side of the LV (see figure 4.6(a)). However, the RV may be located on the other side in some exceptional cases. As shown in figure 4.6(b), the RV is located in the left-lower section compared to the LV. The RV is located in the right-upper part compared to the LV in figure 4.6(c).

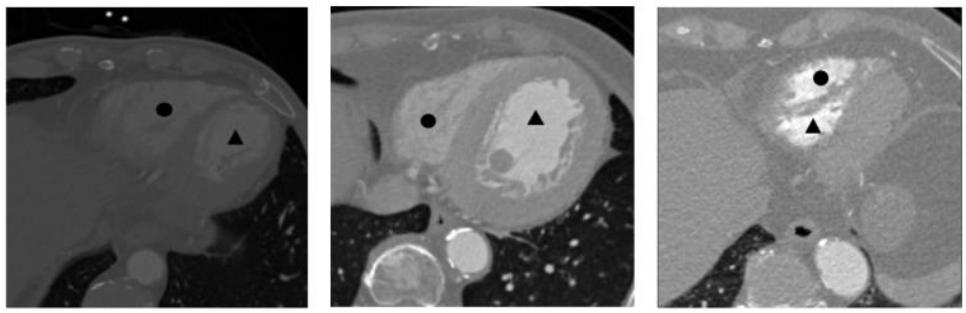

(a) (b) (c)

Figure 4.6 Comparison of the center of the RV (black circle) and LV (black triangle). (a) General case. The RV is located on the left-upper side of the LV. (b) Exceptional Case 1. The RV is located on the left-lower side of the LV. (c) Exceptional Case 2. The RV is located on the right-upper side of the LV.

Therefore, in order to detect the LV and the RV accurately in both the general and exceptional cases, we define the following cost function and examine the value of this cost function:

$$S = Sign(n_0 - n_1) \tag{4.1}$$

where comp1 and comp2 are the largest and second-largest connected components, respectively, and C_x is the centroid of x. $y = mx + n_0$ is the line equation passing C_{comp1} whose slope is m ($m > 0$) and y-intercept is n_0. This line is perpendicular to the line passing C_{comp1} and the center of C_{comp1} and C_{comp2}. In the same manner, n_1 is the y-intercept of the line passing C_{comp2}. If S is negative, comp1 is part of the LV and comp2 is part of the RV. Conversely, if S is positive or zero, comp1 is part of the RV and comp2 is part of the LV. Equation (4.1) is represented with respect to

C_{comp1} and C_{comp2} as follows:

$$S = Sign((C_{Comp1}y + aC_{comp1}x) - (C_{Comp2}y + aC_{comp2}x)) \\ = Sign((C_{Comp1}y - C_{comp2}y) + a(C_{Comp1}x - C_{comp2}x)). \quad (4.2)$$

Figure 4.7 shows this concept with graphic.

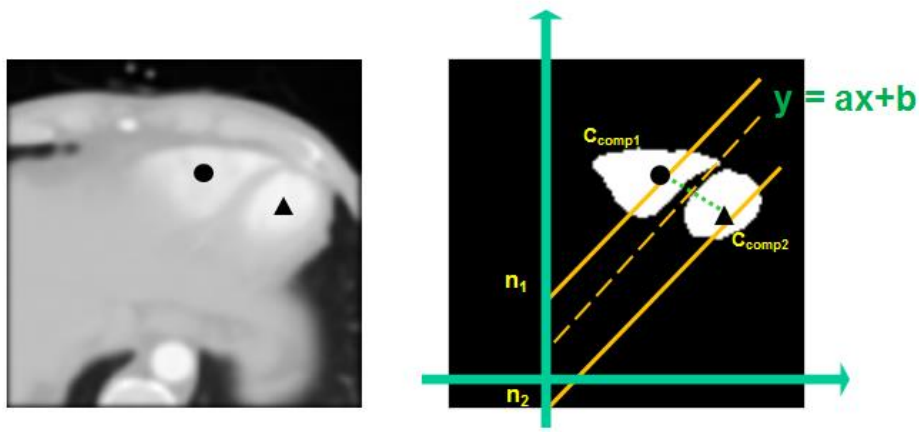

(a) (b)

Figure 4.7 The graphic explanation for separation of left and right sides of heart. (a) Separated heart, the left and right sides. Black circle is right ventricle and triangle is left ventricle. (b) The line equation which is perpendicular to the line passing component1 and cmoponent2.

4.3.2 Detection of Left and Right Sides of Heart

The 3D seed volume of the LV and RV is generated by gathering the 2D seed region of the LV and the RV in each slice. We separate the left and right sides of the

heart by applying a power watershed [24] based on these seed volumes. This divides the segmented whole heart in the previous step into the left and right sides of the heart (see figure 4.8).

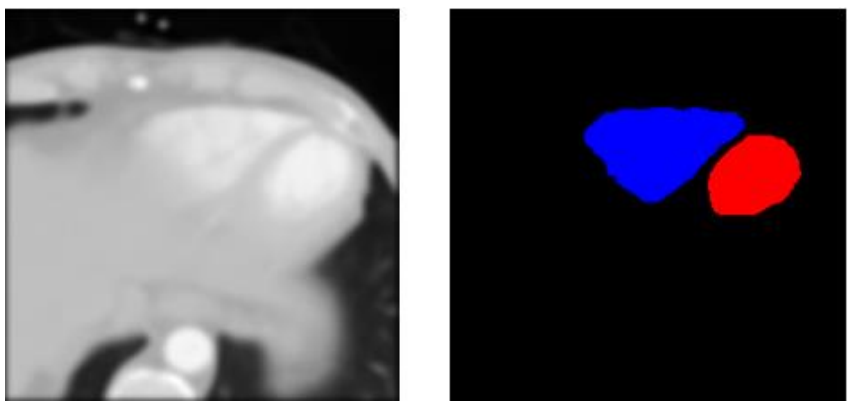

(a) (b)

Figure 4.8 LV and RV in the lower axial slice. (a) Smoothed CT image. (b) Detected LV (red) and RV (blue) region.

A power watershed is a segmentation algorithm used for solving an energy minimization problem based on graph theory. In graph-based image segmentation, an edge weight is assigned to encode nodal similarity such that edges with high weights are considered to be strongly connected and edges with low weights are regarded as weakly connected or nearly disconnected nodes. One common equation for generating weights from image intensities is as follows:

$$\omega_{ij} = \exp(-\beta(\nabla I)^2) \tag{4.3}$$

where ∇I is the normalized gradient of the image I and β is a weighting

coefficient. β was experimentally determined as 1. Figure 4.9 show an example of power watershed based segmentation with five seeds.

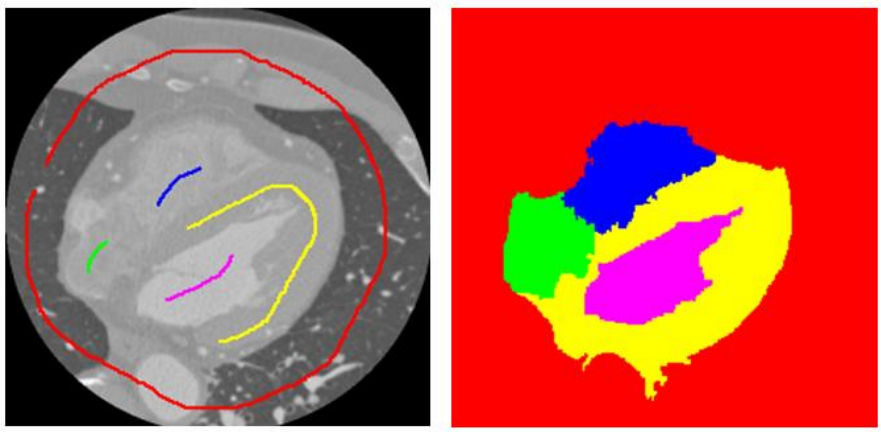

(a) (b)

Figure 4.9 An example of power watershed based segmentation with five seeds. (a) The seeds with manual drawing (red, blue, green, yellow and purple edges). (b) The result of segmentation using power watershed optimization.

For image segmentation in two classes, given foreground FO and background BA seeds, the energy model of the power watershed is given by:

$$
\begin{aligned}
x = \arg\min_{x} \; & \sum_{e_{ij} \in E} \omega^{p}{}_{ij} \, | x_i - x_j |^{q} + \\
& \sum_{v_i} \omega^{p}{}_{Fi} \, | x_i |^{q} + \sum_{vi} \omega^{p}{}_{Bi} \, | x_i - 1 |^{q}, \\
s.t. \;\; & x(FO) = 1, \;\; x(BA) = 0, \\
s_i = 1 \; & if \;\; x_i \geq \frac{1}{2}, \; 0 \;\; if \;\; x_i < \frac{1}{2},
\end{aligned}
\tag{4.4}
$$

where x represents the target configuration, and p and q are values that provide a reference for the different algorithms. This model is represented as a power watershed in $p \to \infty$ and q = 2 [36]. Therefore, we set the foreground seed volume as the candidate region of the LV that was detected in the previous step, and the background seed volume as the candidate region of the RV that was also detected in the previous step. Then, we can separate the left (i.e., LV and LA) and right (i.e., RV and RA) parts of the heart using the power watershed framework (see figure 4.10).

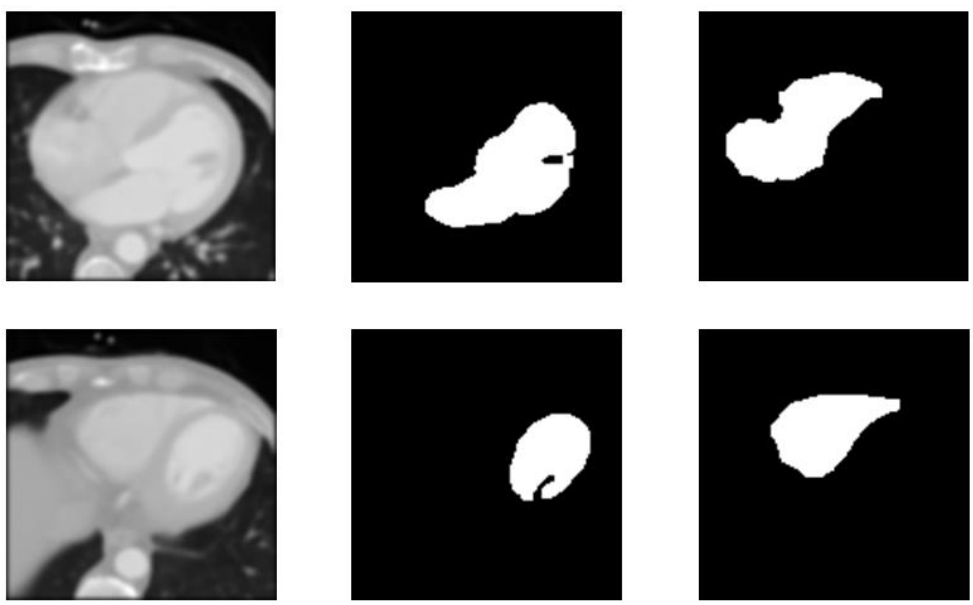

(a) (b) (c)

Figure 4.10 Separation of the left and right sides of the heart. (a) Smoothed CT image. (b) Mask of the left side of the heart. (c) Mask of the right side of the heart.

4.4 Segmentation of Left and Right Sides of Heart

In this step, we segment the left and right sides of the heart accurately using the previous rough segmentation results with GLACM, our proposed method that enhances LACM [31]. LACM uses region-based segmentation that is re-formulated in a local fashion. In general, in region-based segmentation, global image statistics are considered in the entire image. LACM additionally considers local image statistics that are calculated around the propagated contour. Considering the local image statistics allows localized contours to segment objects with heterogeneous features that would be difficult to be segmented correctly using global region-based segmentation. Furthermore, the proposed GLACM considers not only region-based information but also edge-based information for more accurate segmentation compared with LACM.

To segment the heart accurately, we enhance the means separation energy by adding the edge term. The force based on the common edge map has a small capture range because the edge is the local information. In order to extend the capture range, we propose a Gaussian-pyramid edge map. This is a pyramid data structure with the edge map of multi-scale Gaussian-filtered images with different sigma values. The Gaussian-pyramid edge map is generated by accumulating each Gaussian-derivative image with different sigma values. The proposed energy

function of our GLACM is defined as equation (3.14). To segment the left and right sides of the heart based on our model, it is necessary to set the initial contour. We set the initial contour as the rough segmentation results of the LV and RV in the previous step and then we acquire the refined segmentation result of the left and right sides of heart (see figure 4.11).

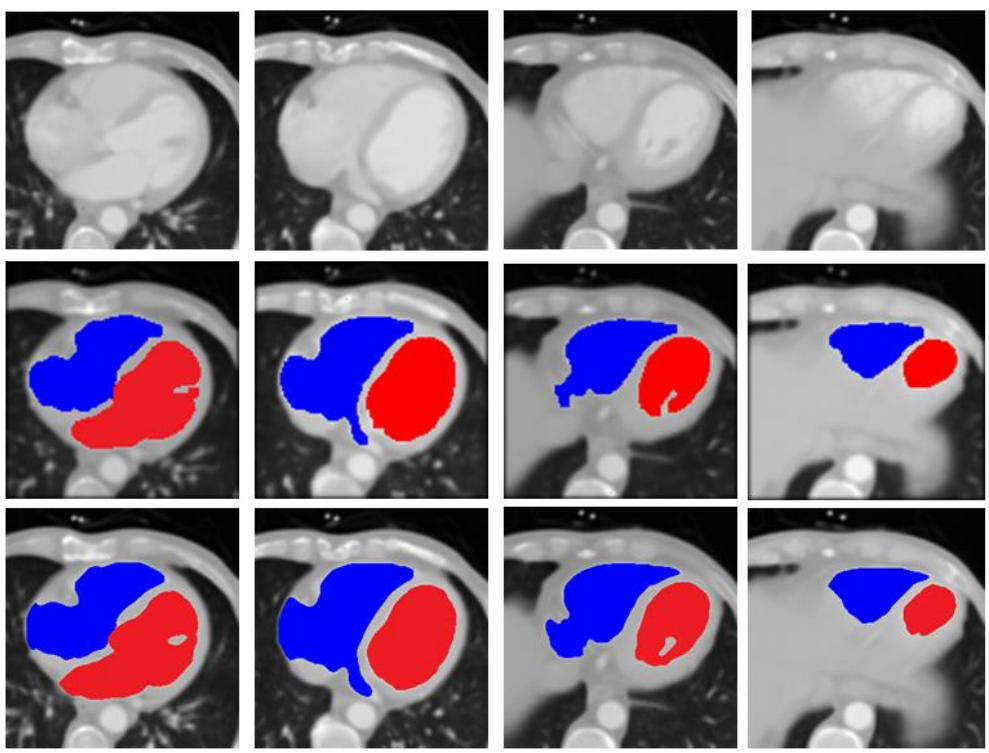

Figure 4.11 Refined segmentation of the left side (red) and the right side (blue) of heart. Smoothed CT image (top), result of separation of the left and right sides of heart (middle), and result of segmentation of the left and right sides of heart (bottom).

4.5 Separation of Atrium and Ventricle from Heart

In this step, we split the left and right sides of the heart into the atrium and ventricle. Because the valve, which separates the atrium and ventricle, is indistinct in the axial slice, we could not exploit the edge-based or region-based segmentation method. In addition, when the valve is open, the boundary line of the ventricle and atrium becomes more ambiguous. In this paper, we propose a two-step procedure for the separation of the atrium and ventricle from the heart with a novel split energy function, which has an area term and an intensity term to split each chamber.

4.5.1 Calculation of Principal Axes of Left and Right Sides of Heart

The heart has a longish ellipsoid shape with a long main axis. We can calculate the direction of this main axis for the left and right sides of the heart by applying principal component analysis (PCA) [40]. PCA is an orthogonal linear transformation that transforms the data to a new coordinate system such that the greatest variance is found by any projection of some axes. The principal components are the eigenvectors of the covariance matrix [40].

We use the position of the mask volume of the segmented left and right sides of the heart in the previous step for the PCA. Since the mask volume is a three-dimensional data structure, the size of a row is ‘3’ and the size of a column is the number of voxels that belong to the mask volume. We compute the eigenvalue and the eigenvector of the matrix using a singular value decomposition [41]. Figure 4.12(a) shows the first principal axis of the left and right sides of the heart. Because it is expected that the axes pass through the separation plane, we detect the plane by minimizing the separating energy function value through the axes in the next step (see figure 4.12(b)).

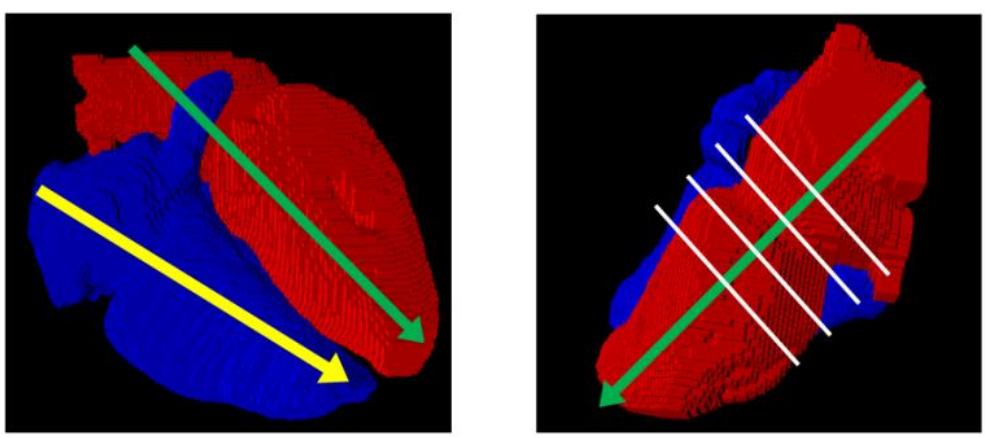

(a) (b)

Figure 4.12 Orientation of heart. (a) First principal axis of left (the green arrow) and right sides of heart (the yellow arrow). (b) Separation planes (the white lines) of left side of heart.

4.5.2 Detection of Separation Plane Using Split Energy Function

Since it is difficult to determine the valve in a cardiac CTA, we find the separation plane approximately located in the valve. To find the separation plane, we first detect the rough location of the plane that separates the right side of the heart. It is easy to search a separation point of the right side of heart because there are intermediate slices where RV and RA are separated. We examine the slices, whether the right side of the heart is separated or not, using 2D connected component analysis. Figure 4.13(a) shows the RV, RA, and their centers, respectively. As shown in figure 4.13(a), the separation point is in the middle of the yellow and blue points. After the separation point of the right side of the heart is detected, we detect the separation point of the left side of the heart by calculating an orthogonal projection point onto the line, orienting the first principal axis, which lies on the first coordinate and has the greatest variance by the projection of the data, and passing through the center of the left side of the heart (see figure 4.13(b)).

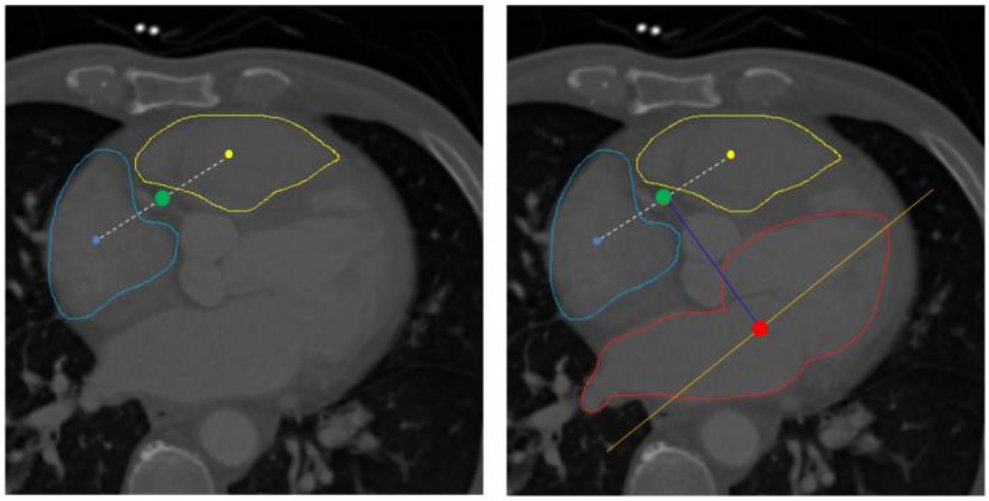

(a) (b)

Figure 4.13 Detection of separation plane. (a) RV (the yellow contour), RA (the blue contour), their centers, and separation point (the green point) of the right side of heart. (b) The separation point (the red point) of the left side of heart.

Although the separation points are detected, they are only approximated candidates since only some of them are the exact points of the separation plane of the left and right sides of the heart. Therefore, we accurately detect the separation planes of the left and right sides of the heart by devising and minimizing a split energy function. We propose a split energy function as follows:

$$E_{sep}(p,\theta,\varphi)=\omega_{area}E_{area}(p,\theta,\varphi)+\omega_{int}E_{int}(p,\theta,\varphi), \quad (4.5)$$

where E_{sep} is the separation energy function, p is a voxel position, and θ and φ are the angles with the second and third principal axis, respectively. ω_{area} and ω_{int} are weights ($\omega_{area} + \omega_{int} = 1$), and E_{area} is the energy term of the area, defined as

follows:

$$E_{area}(p,\theta,\varphi) = \int_{\Omega_M} H(\mathrm{M}(x))\,dx,$$
$$where\ \ H(\mathrm{M}(x)) = \begin{cases} 1, & \mathrm{M}(x) \geq 1 \\ 0, & otherwise \end{cases}, \tag{4.6}$$

where M(x) is the mask volume of the left or right side of the heart, and Ω_M is a plane that passes through the point p with its normal vector oriented toward the angles, θ and φ. E_{int} is the energy term of the intensity, defined as follows:

$$E_{int}(p,\theta,\varphi) = \frac{\int_{\Omega_M} H(M(x))I(x)\,dx}{\int_{\Omega_M} H(M(x))\,dx}, \tag{4.7}$$

where I(x) is the intensity value of the CT image. E_{int} is regarded as the mean intensity of the intercepted plane with the mask volume. We obtain the separation plane by calculating using Powell's method [42]. Once p, θ, and φ are detected, we obtain the normal vector and the position of the plane. This plane is used to split the left or right sides of the heart into the atrium and ventricle. Figure 4.14(b) shows the normal vectors of the separation planes and the direction of the ventricle and atrium. Let $\vec{N}$ = (n_x, n_y, n_z) be the normal vector of the separation

plane, P = (p_x, p_y, p_z) be the point passing through the plane, and V = (v_x, v_y, v_z) be the voxel of the mask volume. We calculate the function value D, defined as follows:

$$\begin{aligned} D(V) &= (\vec{N} \cdot V) - (\vec{N} \cdot P) \\ &= (n_x v_x + n_y v_y + n_z v_z) - (n_x p_x + n_y p_y + n_z p_z), \\ &s.t.,\ M(V) \neq 0. \end{aligned} \tag{4.8}$$

If the function D is positive, the current voxel V belongs to the ventricle. If the function D is negative, the current voxel V belongs to the atrium (see figure 4.14(c)).

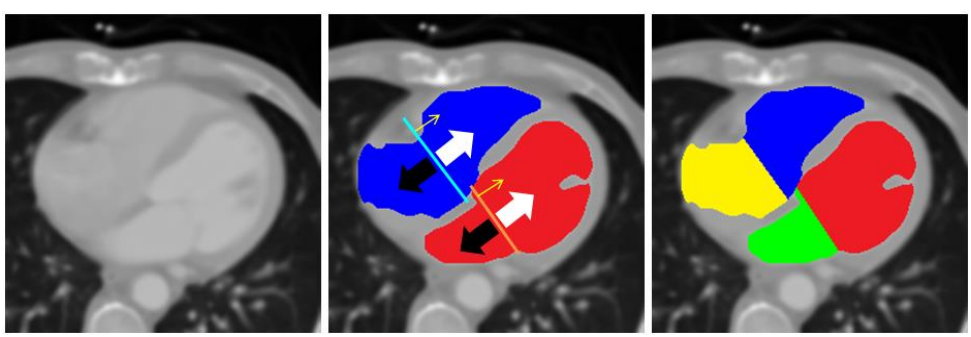

(a) (b) (c)

Figure 4.14 Split of atrium and ventricle by the separation plane. (a) Smoothed CT image. (b) Normal vector (thin yellow vector) of the separation plane, direction of atrium (thick black arrow) and ventricle (thick white arrow). (c) Separation result of atrium and ventricle.

Chapter 5. Experiments

We tested the proposed four-chamber segmentation method using an Intel i7 desktop system with a 3.4 GHz processor and 16 GB of main memory. We implement our method using Microsoft Visual Studio 2008 without the help of other open-source libraries. We prepared twenty clinical scan datasets, each acquired from a different patient. All the datasets were obtained using a cardiac CT scanner by Siemens. The number of images per scan ranged from 183 to 345. Each image had a matrix size of 512 × 512. The voxel size was 0.36 × 0.36 × 0.70 mm.

5.1 Performance Evaluation

To validate the results of the proposed four-chamber segmentation method, we requested a cardiologist with nine years of clinical experience to segment the four chambers manually in each dataset. The cardiologist manually drew the boundary of the four chambers in axial image slices. In this way, we obtained four manually segmented chambers to serve as the ground-truth for the accuracy assessment of the proposed method.

Figure 5.1(a) and (b) show the automatically segmented four chambers

superimposed on axial CT images obtained from the first, second, and third dataset. Figure 5.1(c) shows the 3D surface rendering results of the four-chamber segmentation. LV, LA, RV, and RA are accurately segmented in both 2D and 3D views.

Among the sequential processing steps in the proposed method, we evaluated the accuracy of the proposed method to segment each object including LV, LA, RV, and RA based on four evaluation metrics as follows:

$$E_{fp} = \frac{num\{V_{auto}\} - num\{V_{auto} \cap V_{manual}\}}{num\{V_{manual}\}} \times 100\% \quad (5.1)$$

$$E_{fn} = \frac{num\{V_{manual}\} - num\{V_{auto} \cap V_{manual}\}}{num\{V_{manual}\}} \times 100\% \quad (5.2)$$

$$E_{vol} = \left(\frac{num\{V_{auto}\}}{num\{V_{manual}\}} - 1 \right) \times 100\% \quad (5.3)$$

$$E_{sim} = \left\{ 1 - 2\left(\frac{num\{V_{auto} \cap V_{manual}\}}{num\{V_{auto}\} + num\{V_{manual}\}} \right) \right\} \times 100\% \quad (5.4)$$

where V_{auto} and V_{manual} are the set of voxels in the automatically and manually segmented objects, respectively. The false positive error E_{fp} is the ratio of the set of voxels in the automatically segmented object but not in the manually segmented object to the set of voxels in the manually segmented object. The false negative error E_{fn} is the ratio of the set of voxels in the manually segmented

object but not in the automatically segmented object to the set of voxels in the manually segmented object. The volume measurement error E_{vol} is the ratio between the automatically and manually segmented volumes. The similarity error E_{sim} is defined by the similarity index [43].

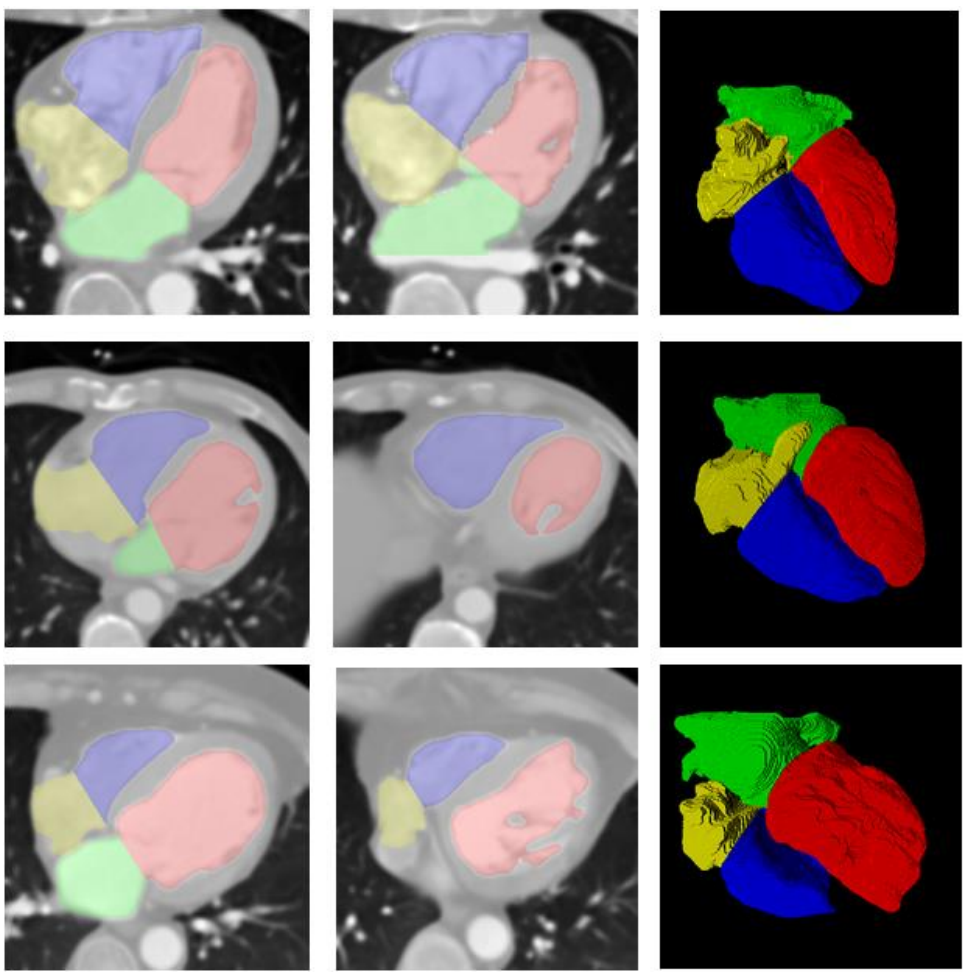

(a) (b) (c)

Figure 5.1 Result of four-chamber segmentation: LV (red area), LA (green area), RV (blue

area), and RA (yellow area). (a) Superimposed image in the upper axial CT slice. (b) Superimposed image in the lower axial CT slice. (c) 3D surface rendering image.

Table 5.1 summarizes the segmentation errors of our four-chamber segmentation for twenty datasets. Each value is the rate of mean ± std. of all the datasets. It shows that Evol of the atrium (i.e., LA and RA) had negative values. Some regions in the atrium were occasionally missed due to the irregular characteristics of the angiography in each atrium. Therefore, Efn was higher than Efp in each atrium. However, the absolute magnitude of Evol of the atrium was less than 5% for all the patients. This shows that the number of missed regions was relatively small. Efp was higher than Efn in each ventricle (i.e., LV and RV). Some regions outside the ventricle were occasionally included. However, similar to the atrium, the amount of falsely included regions was relatively small. In all of the datasets, Esim ranged from 2.1% to 5.5%. The average value of Esim was 3.96±0.94% for all the datasets, indicating that the average differences between the manual and automatic segmentations were less than 5%, approximately.

Table 5.1 Results of accuracy assessment of proposed method

Chamber	E_{fp} (%)	E_{fn} (%)	E_{vol} (%)	E_{sim} (%)
LV	5.34±1.07	2.40±0.70	2.96±0.44	3.82±0.86
LA	2.68±1.20	4.28±1.59	1.60±1.22	3.54±1.28
RV	5.66±1.39	2.94±0.44	2.72±1.28	4.24±0.75
RA	2.40±0.84	5.88±1.18	3.50±0.95	4.24±0.93

For the evaluation of the computational performance of the proposed method, we measured the total processing time. The processing time, averaged over multiple tests for all the datasets, was 46.86±11.37 s. It took 1.62±0.66 s for the segmentation of the whole heart, 6.1±1.3 s for the separation of the left and right sides of the heart, 30.49±6.5 s for the segmentation of the left and right sides of the heart and 8.66±3.06 s for the separation of the atrium and ventricle.

5.2 Comparison with Conventional Method

We compared the proposed method with the Chan-Vese Model (CVM) [30]. This is the state-of-the-art solution for region-based image segmentation [44]. In the CVM, the curve is evolved according to the region-based information of the image to be segmented. Classical CVM uses L^2 norm for the data fidelity [30]. To increase the robustness of the CVM for noise and outliers in the images, a CVM with L^1 norm [29, 45-48] was proposed. In this paper, CVMs with L^1 (CVM_{L1}) and L^2 (CVM_{L2}) norm were used for comparison with the proposed method. In the third step of our proposed method, GLACM was replaced by CVM_{L1} and CVM_{L2} to compare them with our method.

Figure 5.2 and 5.3 show the four-chamber segmentation results using CVM_{L1}, CVM_{L2}, and the proposed method in 2D and 3D views, respectively. Figure 5.2(b), 5.2(e) and 14(a) show the segmentation results using CVM_{L1} from the original CT image in figure 5.2(a). Figure 5.2(c), 5.2(f) and 5.3(b) show the segmentation results using CVM_{L2}. As shown in figures 5.2(c) and 5.2(f), CVM_{L1} and CVM_{L2} falsely include regions outside the heart. In figures 5.2(c) and 5.2(f), the CVM exhibited severe leakages outside the RA and falsely stick to LA (see the circle). This is because it uses the global statistics and considers the intensity of the whole image resulting in the segment of undesired regions. In addition, the

LA and LV are not separated precisely and the boundary of the four chambers is not smooth as shown in figure 5.3(a) and 5.3(b). However, the proposed method accurately segmented the four chambers with smooth boundaries (see figure 5.2(d) and figure 5.3(c)).

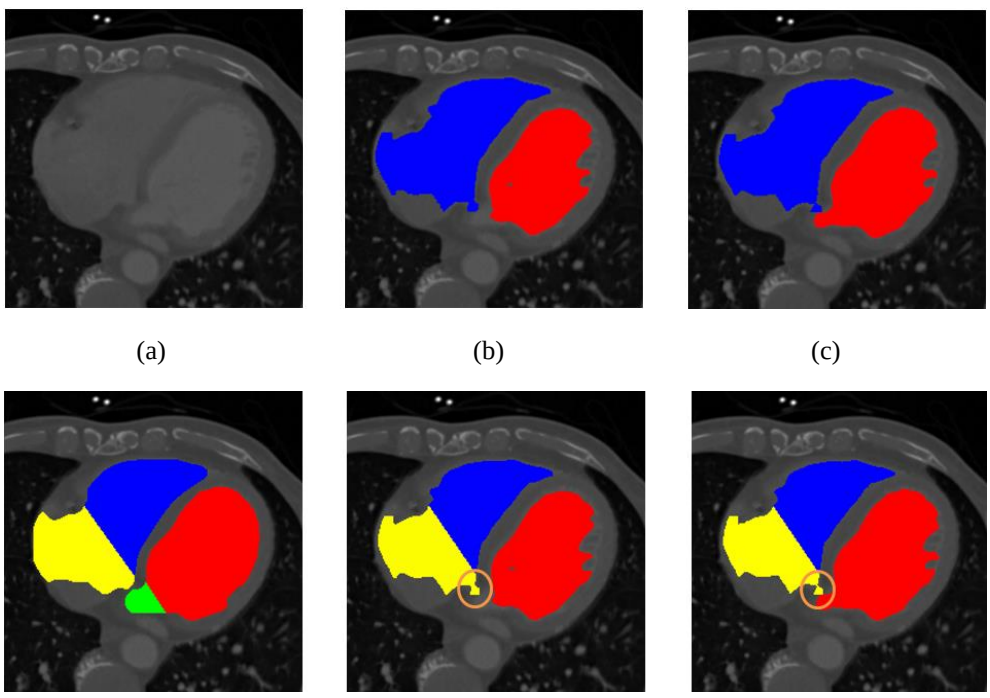

(a) (b) (c)

(d) (e) (f)

Figure 5.2 2D visual comparison of the segmentation results using CVMs and our method: LV (red area), LA (green area), RV (blue area), and RA (yellow area). (a) Original CT image. (b) CVM with L^1 norm before applying split function. (c) CVM with L^2 norm before applying split function. (d) Proposed method. (e) CVM with L^1 norm after applying split function. (c) CVM with L^2 norm after applying split function.

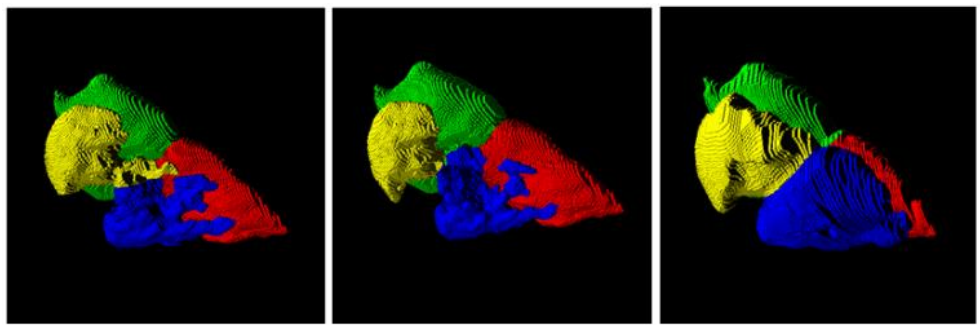

(a) (b) (c)

Figure 5.3 3D visual comparison of the segmentation result using CVMs and our method using 3D surface rendering. (a) CVM_{L1} (b) CVM_{L2} (c) Proposed method.

We compared the segmentation accuracy of the proposed method with those of CVM_{L1} and CVM_{L2} by measuring E_{vol} in (21) and E_{sim} (22) (see table 5.2 and table 5.3). The E_{vol} of the patients using the CVMs had primarily negative values indicating that several regions inside the heart were not segmented. Specifically, some regions in the RV and RA were not included using the CVM. However, these were accurately segmented using the proposed method. The average value of E_{sim} for CVM_{L1} was 12.74% ± 7.40% and CVM_{L2} was 10.25% ± 2.47% for all the datasets, respectively. Although CVM_{L2} showed better performance compared to CVM_{L1}, our proposed method exhibited the most accurate segmentation results with the lowest value of E_{sim}.

Table 5.2 Comparison of segmentation accuracy, E_{vol}

Chamber	*CVM* $_{L1}$	*CVM* $_{L2}$	*Our*
LV	12.92 ± 11.28	15.08 ± 1.34	2.96 ± 0.44
LA	5.92 ± 4.76	0.34 ± 8.28	1.60 ± 1.22
RV	21.60 ± 18.32	7.58 ± 16.31	2.72 ± 1.28
RA	22.76 ± 10.18	6.54 ± 13.17	3.50 ± 0.95

Table 5.3 Comparison of segmentation accuracy, E_{sim}

Chamber	*CVM* $_{L1}$	*CVM* $_{L2}$	*Our*
LV	11.16 ± 2.83	11.02 ± 1.71	3.82 ± 0.86
LA	8.62 ± 1.79	9.04 ± 2.84	3.54 ± 1.28
RV	14.66 ± 12.58	9.82 ± 2.02	4.24 ± 0.75
RA	16.50 ± 6.61	7.42 ± 9.77	4.24 ± 0.93

Figure 5.4 show the four-chamber segmentation results using original LACM and GLACM. The Original LACM falsely sticks to LA (seed the orange circle). On the other hand, GLACM segments each chamber precisely due to Gaussian-pyramid edge map and adaptive radius function.

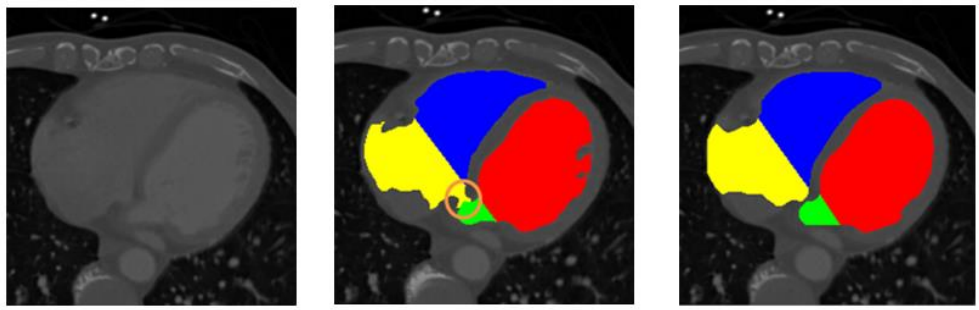

(a) (b) (c)

Figure 5.4 2D visual comparison of the segmentation results using LACM and our method. (a) Original CT image. (b) The result of the segmentation using LACM (c) The result of the segmentation using our proposed method, GLACM.

5.3 Parameter Study

We evaluated the effects of the intensity weight parameter, ω_{int} in (15), of the proposed method on the overall segmentation accuracy. This parameter could influence the separation of the heart into ventricle and atrium since it determines the rotation angles of the principle axes to determine the separation plane. While varying this intensity weight from 0.2 to 1.0, we assessed E_{vol} in (21) and E_{sim} in (22) of the four-chamber segmentation result. Figure 5.5 shows that E_{vol} and E_{sim} are relatively high when the intensity weights are larger than 0.4. Therefore, the optimal parameter value of the intensity weight was determined to be 0.4 with the smallest E_{vol} of 2.7% ± 1.2% and E_{sim} of 4.0% ± 0.9%.

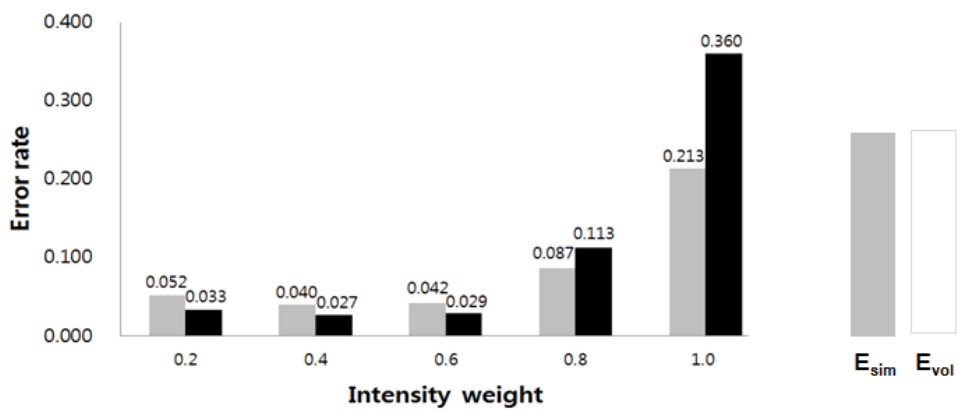

Figure 5.5 E_{sim} (gray) and E_{vol} (black) by varying the parameter of the intensity weight.

5.4 Computational Performance

To evaluate the computational performance, we experiment the processing times for each step of the four-chamber segmentation. The total processing time, averaged over 10 runs to all the datasets, were 71.5 ± 3.3s. The processing time of the first step, segmentation of whole heart, was 12.5 ± 1.6s. And the second step, separation of left and right sides of heart, was 15.1 ± 1.4s. The third step, segmentation of left and right sides of heart, was 35.7 ± 2.5s. Finally, the fourth step, separation of atrium and ventricle form heart, was 8.2 ± 0.7s (see table 5.4). As seen on table 5.4, the third step has largest computation time.

Table 5.4 Results of computational performance

Process	Step				
	First step	Second step	Third step	Fourth step	Total
Time (s)	12.5 ± 1.6s	15.1 ± 1.4s	35.7 ± 2.5s	8.2 ± 0.7s	71.5 ± 3.3s

Chapter 7. Conclusion

This paper presented a novel four-chamber segmentation method using GLACM and a split energy function for cardiac CTA images. First, the whole heart is roughly extracted from a cardiac CTA. This whole heart is roughly separated using a power watershed. Subsequently, the left and right sides of the heart are accurately segmented with the proposed GLACM. The left and right sides of the heart are then separated into atrium and ventricle using a minimizing split energy function.

The four chambers of the heart have ambiguous boundaries and inhomogeneous regions due to the irregular distribution of contrast. For the automatic four-chamber segmentation, we developed a new strategy to extract the left and right sides of the heart, and then divide each of them into the atrium and the ventricle based on the shape and the intensity of the heart. Our method has several outstanding features compared to earlier approaches. As described earlier, each chamber has a weak object boundary. Therefore, it is not easy to extract them from the whole heart region. To segment them accurately, we propose GLACM. This improves upon LACM with a Gaussian-pyramid edge map. It enables the extraction of the desired object accurately from other similar objects adjacent to it by considering both the intensity and gradient. In addition, we present an energy

function of GLACM in terms of the circular region having an adaptively changed radius. This determines the range of segmentation in GLACM for the adaptive capture range. Because in GLACM we consider the points near the contour whose capture range is variable, which means that GLACM considers the local region of the boundary adjacent to other objects, the contour of each chamber is extracted more precisely.

The other outstanding feature of our four-chamber segmentation is that it separates the atrium and the ventricle from the heart by devising a novel split energy function. This feature minimizes the energy function that is combined with the energy term of the area and the intensity. It enables the separation of the ventricle and atrium in the heart, which have a less distinct boundary, by considering both the heart shape and the intensity distribution. The experimental results using clinical datasets demonstrate that the proposed algorithm can accurately and automatically extract the four chambers.

However, this method might fail in specific problematic cases. An example of this would be if the chambers of the heart are missing in the CTA. This occurs due to floating a radio-opaque contrast agent in the blood vessels and the chambers. In such a case, the chambers are invisible and it is impossible to extract them from the heart. The other problematic case is the one in which the shape of the heart has no concave regions, which is where the valves of the ventricle and atrium are located.

In addition, our method would not currently segment the myocardium because its intensity is similar to other muscles or soft tissues. In order to extract the myocardium, it would be necessary to use a statistical method or shape prior information.

We are planning to improve this method to operate robustly even when the CTA has poor contrast or no concave regions. Other image information such as curvature, invariant moments [49-50], or the texture of the heart shape would be helpful to reconstruct the missing part. We will devise the shape term, which has the information of the heart shape and apply it to our energy function.

Bibliography

[1] P. Schoenhagen, A. Stillman, S. Halliburton, and R. White. CT of the heart: principles, advances, clinical uses. Cleveland Clinic journal of medicine, 72(2), pp.127-138, 2005.

[2] World Health Organization. The world health report: Report of the director-general. World Health Organization, 2003.

[3] K. Wong, R. Kelso, S. Worthley, P. Sanders, J. Mazumdar, and D. Abbott. Cardiac flow analysis applied to phase contrast magnetic resonance imaging of the heart. Annals of biomedical engineering, 37(8), pp.1495-1515, 2009.

[4] K. Wong, J. Tu, R. Kelso, S. Worthley, P. Sanders, J. Mazumdar, and D. Abbott. Cardiac flow component analysis. Medical engineering & physics, 32(2), pp.174-188, 2010.

[5] K. Wong, J. Tu, Z. Sun, and D. Dissanayake. Methods in research and development of biomedical devices. World Scientific, 2013.

[6] D. Lesage, E. Angelini, L. Bloch, and G. Funka-Lea. A review of 3D vessel lumen segmentation techniques: Models, features and extraction schemes. Medical image analysis, 13(6), pp.819-845, 2009.

[7] T. Boskamp, D. Rinck, F. Link, B. Kümmerlen, G. Stamm, and P.

Mildenberger. New Vessel Analysis Tool for Morphometric Quantification and Visualization of Vessels in CT and MR Imaging Data Sets 1. Radiographics, 24(1), pp.287-297, 2004.

[8] J. Mille, and L. Cohen, (2009, June). Deformable tree models for 2D and 3D branching structures extraction. In Computer Vision and Pattern Recognition Workshops, 2009. CVPR Workshops 2009. IEEE Computer Society Conference on, pp. 149-156, Jun, 2009.

[9] V. Luboz, X. Wu, K. Krissian, C. Westin, R. Kikinis, S. Cotin, and S. Dawson. A segmentation and reconstruction technique for 3D vascular structures. In Medical Image Computing and Computer-Assisted Intervention–MICCAI 2005, Springer Berlin Heidelberg, pp. 43-50, 2005.

[10] A. Frangi, W. Niessen, and M. Viergever. Three-dimensional modeling for functional analysis of cardiac images, a review. Medical Imaging, IEEE Transactions on, 20(1), pp.2-5, 2001.

[11] S. Abadi, A. Roguin, A. Engel, and J. Lessick. Feasibility of automatic assessment of four-chamber cardiac function with MDCT: Initial clinical application and validation. European journal of radiology, 74(1), pp.175-181, 2010.

[12] H. Kirisli, M. Schaap, S. Klein, L. Neefjes, A. Weustink, T. Van Walsum, and W. Niessen. Fully automatic cardiac segmentation from 3D CTA

data: a multi-atlas based approach. In SPIE Medical Imaging, International Society for Optics and Photonics, pp. 762305-762305, March, 2010.

[13] J. Tan, E. Ng, and R. Acharya. An efficient automated algorithm to detect ocular surface temperature on sequence of thermograms using snake and target tracing function. Journal of medical systems, 35(5), pp.949-958, 2011.

[14] K. Wong, Z. Sun, J. Tu, S. Worthley, J. Mazumdar, and D. Abbott. Medical image diagnostics based on computer-aided flow analysis using magnetic resonance images. Computerized Medical Imaging and Graphics, 36(7), pp.527-541, 2012.

[15] J. Tan, E. Ng, and U. Acharya. Automated detection of eye and cornea on infrared thermogram using snake and target tracing function coupled with genetic algorithm. Quantitative InfraRed Thermography Journal, 6(1), pp.21-36, 2009.

[16] K. Wong, R. Kelso, S. Worthley, P. Sanders, J. Mazumdar, and D. Abbott. Medical imaging and processing methods for cardiac flow reconstruction. Journal of Mechanics in Medicine and Biology, 9(01), pp.1-20, 2009.

[17] T. Cootes, C. Taylor, D. Cooper, and J. Graham. Active shape models-their training and application. Computer vision and image understanding,

61(1), pp.38-59, 1995.

[18] T. Cootes, G. Edwards, and C. Taylor. Active appearance models. IEEE Transactions on pattern analysis and machine intelligence, 23(6), pp.681-685, 2001.

[19] O. Ecabert, J. Peters, and J. Weese. Modeling shape variability for full heart segmentation in cardiac computed-tomography images. In Medical Imaging, International Society for Optics and Photonics. pp. 61443R-61443R, March, 2006.

[20] K. Park, A. Montillo, D. Metaxas, and L. Axel. Volumetric heart modeling and analysis. Communications of the ACM, 48(2), pp.43-48, 2005.

[21] H. Van Assen, M. Danilouchkine, M. Dirksen, J. Reiber, and B. Lelieveldt. A 3-D active shape model driven by fuzzy inference: application to cardiac CT and MR. Information Technology in Biomedicine, IEEE Transactions on, 12(5), pp.595-605, 2008.

[22] T. Takagi, and M. Sugeno. Fuzzy identification of systems and its applications to modeling and control. Systems, Man and Cybernetics, IEEE Transactions on, (1), pp.116-132, 1985.

[23] S. Mitchell, J. Bosch, B. Lelieveldt, R. van der Geest, J. Reiber, and M. Sonka. 3-D active appearance models: segmentation of cardiac MR and

ultrasound images. Medical Imaging, IEEE Transactions on, 21(9), pp.1167-1178, 2002.

[24] O. Ecabert, J. Peters, H. Schramm, C. Lorenz, J. von Berg, M. Walker, and J. Weese. Automatic model-based segmentation of the heart in CT images. Medical Imaging, IEEE Transactions on, 27(9), pp.1189-1201, 2008.

[25] G. Funka-Lea, Y. Boykov, C. Florin, M. Jolly, R. Moreau-Gobard, R. Ramaraj, and D. Rinck. Automatic heart isolation for CT coronary visualization using graph-cuts. In Biomedical Imaging: Nano to Macro, 2006. 3rd IEEE International Symposium on, pp. 614-617, April, 2006.

[26] L. Grady, V. Sun, and J. Williams. Interactive graph-based segmentation methods in cardiovascular imaging. In Handbook of mathematical models in computer vision, Springer US, pp. 453-469, 2006.

[27] Y. Zheng, A. Barbu, B. Georgescu, M. Scheuering, and D. Comaniciu. Four-chamber heart modeling and automatic segmentation for 3-D cardiac CT volumes using marginal space learning and steerable features. Medical Imaging, IEEE Transactions on, 27(11), pp.1668-1681, 2008.

[28] S. Zhang, Y. Zhan, M. Dewan, J. Huang, D. Metaxas, and X. Zhou. Towards robust and effective shape modeling: Sparse shape composition. Medical image analysis, 16(1), pp.265-277, 2012.

[29] O. Rousseau, and Y. Bourgault. Heart segmentation with an iterative Chan-Vese algorithm. HAL Preprint. hal-00403627, 2009.

[30] T. Chan, and L. Vese. Active contours without edges. Image processing, IEEE transactions on, 10(2),pp. 266-277, 2001.

[31] S. Lankton, and A. Tannenbaum. Localizing region-based active contours. Image Processing, IEEE Transactions on, 17(11), pp.2029-2039, 2008.

[32] L. Rudin, S. Osher, and E. Fatemi. Nonlinear total variation based noise removal algorithms. Physica D: Nonlinear Phenomena, 60(1), pp.259-268, 1992.

[33] N. Otsu. A threshold selection method from gray-level histograms. Automatica, 11(285-296), pp.23-27, 1975.

[34] T. Kanungo, D. Mount, N. Netanyahu, C. Piatko, R. Silverman, and A. Wu. An efficient k-means clustering algorithm: Analysis and implementation. Pattern Analysis and Machine Intelligence, IEEE Transactions on, 24(7), pp.881-892, 2002.

[35] C. Couprie, L. Grady, L. Najman, and H. Talbot, Power watershed: A unifying graph-based optimization framework. Pattern Analysis and Machine Intelligence, IEEE Transactions on, 33(7), pp.1384-1399, 2011.

[36] A. Sinop, and L. Grady, A seeded image segmentation framework unifying graph cuts and random walker which yields a new algorithm.

Proceedings of 11th International Conference on Computer Vision, pp.1-8, October, 2007.

[37] S. Osher, and R. Fedkiw. Level set methods and dynamic implicit surfaces. Springer, US, 2003.

[38] R. Tsai, and S. Osher. Review article: Level set methods and their applications in image science. Communications in Mathematical Sciences. 1(4), pp.1-20, 2003.

[39] A. Yezzi Jr, A. Tsai, and A. Willsky. A fully global approach to image segmentation via coupled curve evolution equations. Journal of Visual Communication and Image Representation. 13(1), pp.195-216, 2002.

[40] J. Shlens. A tutorial on principal component analysis. Systems Neurobiology Laboratory, University of California at San Diego, pp.1-12, 2005.

[41] W. Press. Numerical recipes 3rd edition: The art of scientific computing. Cambridge university press, 2007.

[42] M. Powell. An efficient method for finding the minimum of a function of several variables without calculating derivatives. The Computer Journal. 7(2), pp.155-162, 1964.

[43] A. Zijdenbos, B. Dawant, R. Margolin, and A. Palmer. Morphometric analysis of white matter lesions in MR images: method and validation.

Medical Imaging, IEEE Transactions on, 13(4), pp.716-724, 1994.

[44] S. Bukhari, F. Shafait, and T. Breuel. Segmentation of curled textlines using active contours. Proceedings of The Eighth IAPR International Workshop on Document Analysis Systems, pp.270-222, September, 2008.

[45] S. Alliney. Digital filters as absolute norm regularizers. Signal Processing , IEEE Transactions on, 40(6), pp.1548-1562, 1992.

[46] S. Alliney. Recursive median filters of increasing order: A variational approach. Signal Processing, IEEE Transactions on, 44(6), pp.1346-1354, 1996.

[47] S. Alliney. A property of the minimum vectors of a regularizing functional defined by means of the absolute norm. Signal Processing, IEEE Transactions on, 45(4), pp.913-917, 1997.

[48] M. Nikolova. A variational approach to remove outliers and impulse noise. Journal of Mathematical Imaging and Vision. 20(1-2), pp.99-120, 2004.

[49] J. Flusser, B. Zitova, and T. Suk. Moments and moment invariants in pattern recognition. Wiley, US, 2009.

[50] M. Hu. Visual pattern recognition by moment invariants. IRE Transactions on Information Theory, 8(2), pp.179-187, 1962.

[51] G. Thibodeau, K. Patton. STRUCTURE & FUNCTION OF THE BODY.

12th Edition, Mosby, 2004.

[52] M. Heath, S. Sarkar, T. Sanocki, and K. Bowyer. A robust visual method for assessing the relative performance of edge-detection algorithms. Pattern Analysis and Machine Intelligence, IEEE Transactions on, 19(12), pp.1338-1359, 1997.

[53] J. Canny. A computational approach to edge detection. Pattern Analysis and Machine Intelligence, IEEE Transactions on, (6), pp.679-698, 1986.

[54] H. Yuen, J. Princen, J. Illingworth, and J. Kittler. Comparative study of Hough transform methods for circle finding. Image and Vision Computing, 8(1), pp.71-77, 1990.

[55] R. Adams, and L. Bischof. Seeded region growing. Pattern Analysis and Machine Intelligence, IEEE Transactions on, 16(6), pp.641-647, 1994.

[56] M. Kass, A. Witkin, and D. Terzopoulos. Snakes: Active contour models. International journal of computer vision, 1(4), pp.321-331, 1988.

[57] S. Osher, and J. Sethian. Fronts propagating with curvature-dependent speed: algorithms based on Hamilton-Jacobi formulations. Journal of computational physics 79(1), pp.12-49, 1988.

[58] N. Paragios, Geodesic active regions and level set methods:

Contributions and applications in artificial vision. Dissertation, University of Oxford, UK, 2000.

[59] R. Ronfard, Region-based strategies for active contour models. International Journal of Computer Vision, 13(2), pp.229-251, 1994.

[60] S. Zhu, and A. Yuille. Region competition: Unifying snakes, region growing, and Bayes/MDL for multiband image segmentation. Pattern Analysis and Machine Intelligence, IEEE Transactions on, 18(9), pp.884-900, 1996.

[61] D. Mumford and J. Shah, Optimal Approximations by Piecewise Smooth Functions and Associated Variational Problems. Communications on Pure and Applied Mathematics, 42(5), pp.577-685, 1989.

[62] Jr. Yezzi, A. Tsai, and A. Willsky. A statistical approach to snakes for bimodal and trimodal imagery. In Computer Vision, 1999. The Proceedings of the Seventh IEEE International Conference on, 2, pp. 898-903, 1999.

[63] A. Amini, T. Weymouth, and R. Jain. Using dynamic programming for solving variational problems in vision. Pattern Analysis and Machine Intelligence, IEEE Transactions on, 12(9), pp.855 –867, 1990.

[64] A. Falcão, J. Udupa, S. Samarasekera, S. Sharma, B. Hirsch, and R. Lotufo. User-steered image segmentation paradigms: Live wire and live lane. Graphical models and image processing, 60(4), pp.233-260, 1998.

[65] D. Geiger, A. Gupta, L. Costa, and J. Vlontzos, Dynamic programming for detecting, tracking, and matching deformable contours. Pattern Analysis and Machine Intelligence, IEEE Transactions on, 17(3), pp.294 –302, 1995.

[66] E. Mortensen, and W. Barrett, Interactive segmentation with intelligent scissors. Graphical Models and Image Processing, 60(5), pp.349–384, 1998.

[67] Y. Boykov, and M. Jolly. Interactive graph cuts for optimal boundary & region segmentation of objects in ND images. In Computer Vision, 2001. ICCV 2001. Proceedings. Eighth IEEE International Conference on, 1, pp.105-112, 2001.

[68] Y. Boykov, and G. Funka-Lea. Graph cuts and efficient ND image segmentation. International journal of computer vision, 70(2), pp.109-131, 2006.

[69] D. Pham, C. Xu, and J. Prince. Current methods in medical image

segmentation 1. Annual review of biomedical engineering, 2(1), pp.315-337, 2000.

[70] J. Peters, O. Ecabert, C. Meyer, H. Schramm, R. Kneser, A. Groth, and J. Weese. Automatic whole heart segmentation in static magnetic resonance image volumes. In Medical Image Computing and Computer-Assisted Intervention–MICCAI 2007, Springer Berlin Heidelberg, pp.402-410, 2007.

초 록

심장은 인체에서 가장 중요한 기관 중 하나이고 복잡한 구조로 구성되어 있다. 컴퓨터 단층 촬영 영상, 자기 공명 영상, 그리고 단일광자방출단층촬영은 비 침습 심장 영상 모달리티로 많이 사용 된다. 심장의 컴퓨터 단층 촬영 혈관 조영 영상은 다른 모달리티 영상과 비교하여 높은 공간적 해상도를 가지고 있기 때문에 보다 많고 자세한 해부학적 정보, 심장의 각 챔버, 혈관, 관상동맥 등을 제공한다. 심장의 중요한 형태학적 정보를 얻기 위해서는 심장 영역을 분할하는 과정이 필요하고 임상적 진료에 사용될 수 있다. 영상 분할은 영상을 의미 있는 부분으로 나누는 문제로 의료 영상 분야의 경우 기관의 체적을 측정하기 위해 사용된다. 본 연구에서는 심장의 각 챔버를 자동으로 분할하는 새로운 기법을 제안한다. 첫 번째로 심장의 컴퓨터 단층 촬영 영상으로부터 심장의 영역을 대략적으로 분할 한다. 이때 분할된 심장 영역은 해부학적 정보를 기반으로 한 기하학적 분석과 멱 분수계 방식을 이용하여 좌측과 우측 심장으로 나뉜다. 그 다음 본 연구에서 제안하는 심장 컴퓨터 단층촬영 영상으로부터 경사도가 추가된 지역 능동 윤곽 모델을 이용하여 심장의 좌측과 우측을 정밀하게 추출한다. 마지막으로 전 단계에서 분할 된 좌측과 우측 심장들은 본 연구에서 제안하는 분리 에너지 함수를 이용하여 각각 심방과 심실로 나누어 지게 된다. 분리 에너지 함수는 각 심장에서 심방과 심실을 나누는 기준이 되는 벨브를 영상에서 심장의 모양과 밝기 값을 이용하여 분리 에너지 함수가 최소화 되는 분할 평면을 찾는다. 심장 분할에서 우리가 해결해야 할 부분은 약한 에지나 구분자를 가진 심장 영상에서 각 챔버를 분할해야 한다는 점이다. 이질적 영역에서의 심장 분할 시 정확성을

높이기 위해 지역 정보와 에지 정보를 사용하였다. 심장 분할을 위한 방법 중 많은 학습 데이터와 기준 모델이 필요한 모델 기반 방식이 주로 사용되어 왔다. 모델 기반 방식에서 학습 데이터는 정확한 심장 영역을 나타내야 하고 분할을 정확히 하기 위해 많은 수의 데이터들이 사용 되어야 하기 때문에 모델 기반 방식을 사용하는 것은 쉽지 않다. 게다가 학습 데이터는 뚜렷한 특징점으로 표현되어야 하고 각 데이터 간의 특징점은 일관성을 가져야 하며 손으로 직접 설정해 주어야 한다. 하지만 본 연구에서는 학습 데이터와 기준 모델 대신 심장 영상으로부터 에지, 밝기 값, 형태 정보 등을 얻어 분할에 사용한다. 밝기 정보는 기준 모델의 형태 정보를 대체 할 수 있다. 또한 에지 정보를 효과적으로 이용하고 기존의 지역 능동 윤곽 모델보다 분할 정확성을 높이기 위해 적응 반지름 함수와 가우시안 피라미드 에지 맵을 고안하였다. 지역 능동 윤곽 모델에서는 밝기 값을 비교하는 반지름의 크기가 분할 성능에 영향을 미치기 때문에 영상의 성질에 맞게 반지름을 변화 시키면서 적용한다. 심장의 심방과 심실을 나누는 밸브를 검출하기 위한 분리 에너지 함수도 제안하였다. 심장 영상에서 밸브는 애매하고 불명확한 에지를 가지고 있기 때문에 밸브를 검출하기가 쉽지 않다. 본 연구에서는 밸브를 검출하기 위해 심방과 심실이 맞닿은 부분의 형태와 밝기 정보를 이용한다. 실험에서 20개의 데이터를 사용하여 본 연구에서 제안하는 방법을 이용하여 심장의 각 챔버를 정확하고 효과적으로 분할하였음을 보였고 심장 전문의의 임상학적 조사와 기능에 도움을 줄 수 있음을 보였다.

주요어: 심장 분할, 영역 분할, 지역 능동 윤곽 모델, 에지 맵, 분리 에너지 함수
학번: 2009-30909